



Contents lists available at ScienceDirect

## Journal of Quantitative Spectroscopy and Radiative Transfer

journal homepage: [www.elsevier.com/locate/jqsrt](http://www.elsevier.com/locate/jqsrt)

# The atmospheric radiative transfer simulator ARTS, version 2.6 — Deep python integration

Stefan A. Buehler<sup>a</sup>,<sup>\*</sup>, Richard Larsson<sup>a</sup>, Oliver Lemke<sup>a</sup>, Simon Pfreundschuh<sup>b</sup>, Manfred Brath<sup>a</sup>, Ian Adams<sup>c</sup>, Stuart Fox<sup>d</sup>, Florian E. Roemer<sup>a</sup>, Paulina Czarnecki<sup>e</sup>, Patrick Eriksson<sup>b</sup>

<sup>a</sup> Meteorological Institute, Center for Earth System Research and Sustainability (CEN), University of Hamburg, Hamburg, Germany

<sup>b</sup> Department of Space, Earth and Environment, Chalmers University of Technology, Gothenburg, Sweden

<sup>c</sup> Mesoscale Atmospheric Processes Laboratory, NASA Goddard Space Flight Center, Greenbelt, MD, United States

<sup>d</sup> Met Office, FitzRoy Road, Exeter, EX1 3PB, UK

<sup>e</sup> Columbia University, New York, NY, United States

## ARTICLE INFO

### Keywords:

Atmospheric radiative transfer simulator  
ARTS  
Absorption  
Scattering  
Line-by-line  
Energy fluxes

## ABSTRACT

The atmospheric radiative transfer simulator ARTS is a software for computing atmospheric absorption, scattering, the transfer of radiation through an atmosphere, and sensor characteristics. It is written in C++ and can simulate remote sensing observations and radiative energy fluxes. The article describes version 2.6 of the software. There are numerous changes compared to the last ARTS publication, the most striking being that the program is now controlled by Python scripts, which is convenient and allows for great flexibility. The article discusses the ARTS history, the theory behind the computations of absorption and radiative transfer, available solvers for atmospheres with scattering, the computation of energy fluxes and heating rates, and the built-in system for inverting remote observations to atmospheric state variables by optimal estimation. ARTS is publicly available, open source, and free of charge.

## 1. Introduction

### 1.1. Basics

The Atmospheric Radiative Transfer Simulator ARTS is a software, written primarily in C++, for calculating atmospheric absorption and scattering, and for simulating the transfer of radiation through planetary atmospheres. Philosophically, what sets it apart from other such programs is its very wide scope and its flexibility, unmatched by any other software that the authors are aware of.

ARTS can do radiative transfer simulations in 1D, 2D, and 3D spherical atmospheres, spherical geometry being a key feature for simulating limb observations. It is used for simulating remote sensing observations and retrieval, but also to compute radiative fluxes and heating rates as a reference for faster radiation schemes in atmospheric circulation models for climate research and weather forecasting.

The radiative transfer is fully polarized, allowing simulation of up to four Stokes components, which is important for simulating sensors with polarization capabilities, and even sometimes for correctly simulating simple polarization sensors observing at frequencies where the radiation is polarized, for example by Zeeman splitting.

ARTS also does analytical or semi-analytical Jacobians (derivatives of the simulated observation with respect to changes in atmospheric state or model parameters), and these can be used in a built-in optimal estimation method (OEM) implementation for atmospheric state retrieval.

A significant part of ARTS deals with the calculation of absorption spectra from line-by-line spectroscopic data catalogues. In line with the overall philosophy, also this part is very flexible, allowing for example calculations with broadening gases other than air, to the extent that broadening parameters are available. This is important for simulating radiation on other planets.

Additionally, other types of absorption can be added, including predefined continua, measured absorption cross-sections, and collision-induced absorption spectra.

For simulations with scattering, a number of different scattering solvers are available, including a native scheme based on lambda-iteration (DOIT), a native Monte-Carlo scheme, and also well-known schemes such as DISORT. There also is a sophisticated system for specifying the single scattering properties that are needed for these simulations.

\* Corresponding author.

E-mail address: [stefan.buehler@uni-hamburg.de](mailto:stefan.buehler@uni-hamburg.de) (S.A. Buehler).

<https://doi.org/10.1016/j.jqsrt.2025.109443>

Received 2 May 2024; Received in revised form 18 February 2025; Accepted 17 March 2025

Available online 31 March 2025

0022-4073/© 2025 The Authors. Published by Elsevier Ltd. This is an open access article under the CC BY license (<http://creativecommons.org/licenses/by/4.0/>).

## 1.2. History

Historically, ARTS started in 2000 as a collaboration between Patrick Eriksson (Chalmers) and Stefan Buehler (then University of Bremen). The program was open source from the start and many others have made important contributions over the years.

Important early milestones were the addition of water vapor continuum absorption by Thomas Kuhn [1] and the iterative scattering solver by Claudia Emde and Sreerekha T. R. [2,3]. Eriksson et al. [4] describes the first OEM implementation (in Matlab) and Buehler et al. [5] gives the first ARTS overview.

Cory Davis [6] added a Monte Carlo scattering solver and Christian Melsheimer [7] did a first validation and intercomparison with other radiative transfer models. Buehler et al. [8] describes the first application of ARTS for radiative flux and cooling rate calculations, and Eriksson et al. [9] developed the matrix sensor representation that is still in use today. Buehler et al. [10] developed a method to represent integral radiation quantities by a few representative frequencies, Buehler et al. [11] describes the handling of absorption in lookup tables, and Eriksson et al. [12] is the second ARTS overview paper.

In 2014, Richard Larsson added code to handle Zeeman splitting [13,14]. This code was revised over the years and Zeeman splitting coefficients were updated for oxygen and other species [15,16].

For calculations with ice particle scattering, dedicated databases of single scattering data for different particle shapes and sizes were developed for ARTS for both randomly oriented [17] and specifically oriented [18] particles. Very recently, polynomial fits to HITRAN absorption cross-section data [19] were developed to allow simulations with a large number of halocarbon species [20].

In general, ARTS release versions have an even last digit, development versions an odd last digit. The most recent ARTS overview paper was [21], describing Version 2.2, and this article is about Version 2.6. The most user-visible change between these versions is the Python integration, but there also have been numerous other improvements, such as a new core to calculate atmospheric absorption, updates to the clear-sky radiative transfer core, new scattering solvers, and the capability to do optimal estimation retrievals inside ARTS. Tables 1 and 2 concisely list the most notable changes from 2.2 to 2.4 (Table 1) and from 2.4 to 2.6 (Table 2).

## 1.3. ARTS use — literature analysis

It is interesting to see for what applications ARTS is used in practice. For this, we did a search on Web of Science for all articles that cite one of the three primary ARTS papers [5,12,21], between 2018 and June 2023. This yielded 134 publications. Out of these, 29 just mention the program. Often they are about other radiative transfer software (for example [22,23]) or spectroscopy (for example [24,25]).

The remaining 105 publications actually used ARTS for their work. The largest group of these (52 publications) deals with remote sensing of the clear atmosphere (without scattering in the radiative transfer setup). Out of these, many used ground-based microwave radiometers for profiles of atmospheric trace gases and temperature. Examples include tropospheric water [26], stratospheric and mesospheric water [27–30], stratospheric and mesospheric ozone [31–35], mesospheric carbon monoxide [36–38], temperature [39,40], and wind [38,41].

Another significant group, still within the clear-sky category, are publications with existing or planned satellite sensors, with examples including operational meteorological microwave and infrared sounders [20,42–49] and microwave to infrared limb sounders [16,50–56]. In addition to these, yet another interesting clear-sky application is the retrieval of the rotational temperature from stratospheric and lower thermospheric O<sub>2</sub> airglow emissions [57,58].

The other big group of publications that used ARTS (38 publications out of 105) deals with all-sky observations of the atmosphere

**Table 1**  
Changes between ARTS 2.2 (described in last overview paper [21]) and ARTS 2.4 (last release).

Key changes between 2.2 and 2.4	Other changes worth mentioning
<ul style="list-style-type: none"> <li>• New improved format for line-by-line data</li> <li>• Non-LTE (pure-rotational non-overlapping, and non-chemical cases)</li> <li>• Dedicated methods for heating rate calculations (see Section 5)</li> <li>• Basic simulations of radars (both single and multiple scattering, see Section 4.2.2)</li> <li>• Radio link calculations not supported in this version</li> <li>• Interfaces to DISORT and RT4 scattering solvers (see Section 4.2)</li> <li>• Jacobian for new quantities: spectroscopic variables and particle properties (hybrid solver, see Section 4.2)</li> <li>• Optimal estimation inversions inside ARTS (see Section 6)</li> <li>• TELSEM and TESSEM surface models</li> <li>• PyARTS: Python bindings for ARTS</li> </ul>	<ul style="list-style-type: none"> <li>• Radiative transfer code (except Monte Carlo) completely revised, including: higher consistency between modules, higher calculation efficiency, Jacobian of atmospheric variables now fully analytical</li> <li>• Absorption code revised: support for new line shapes, performance improvements (see Section 3)</li> <li>• New and extended system for defining particle size distributions (see Section 4.1)</li> <li>• DOIT scattering solver improvements: optimized pressure grid, convergence acceleration, optional precalculated first-guess field</li> <li>• New sensor setup for passband-type meteorological millimeter instruments (sensor_responseMetMM)</li> <li>• New single scattering database for randomly oriented [17] and specifically oriented [18] ice particles</li> </ul>

**Table 2**  
Changes between ARTS 2.4 (last release) and ARTS 2.6 (this version).

Key changes between 2.4 and 2.6	Other changes worth mentioning
<ul style="list-style-type: none"> <li>• Extension to shortwave radiation (see Section 2.2), including new clear-sky solver with support for shortwave radiation (iyClearsky), and addition of molecular scattering (clear-sky Rayleigh scattering)</li> <li>• Support of measured cross-section data (e.g. HITRAN absorption cross-sections, see [20] for details)</li> <li>• Improved DISORT interface</li> <li>• Much improved Python integration, including examples (see Section 1.4)</li> </ul>	<ul style="list-style-type: none"> <li>• Improved flux calculations with DISORT (faster, easier and more accurate)</li> <li>• Recent Rosenkranz absorption models added (PWR2021)</li> <li>• MT_CKD 4.0 Water continuum added</li> <li>• Automatic download of ARTS spectral line catalog (see example in Section 1.4)</li> <li>• New workspace method surfaceFlatRvRhEvEh, to calculate 'surface_rmatrix' and 'surface_emission' when emissivity and reflectance are provided externally.</li> </ul>

and/or the retrieval of hydrometeor properties, so they require radiative transfer simulations with scattering. Applications here include passive microwave to sub-mm wave sensors, radars, and their synergy [59–74]. ARTS is here not only used on its own, but also as a reference to train or validate faster more approximative models, in particular for data assimilation in numerical weather prediction [e.g., 47, 75]. Many studies are in preparation of the upcoming Ice Cloud Imager (ICI) mission on Metop Second Generation [76–79]. Also, several focus specifically on polarized observations [17,18,80,81]. Other studies focus on terahertz sensors [82–86] or on infrared sensors [87].

A growing application area is the simulation of atmospheric infrared energy fluxes and associated heating rates in the context of climate modeling [20,88–91]. Although ARTS so far was not capable of simulating radiative transfer in the solar part of the spectrum, a few studies used its capability to compute atmospheric absorption at these frequencies [92–94].

The overwhelming majority of use is for Earth, but there are also reported applications for Venus [95] and Mars [96]. Also, while the overwhelming majority of studies is in the context of atmospheric science, there is reported use for retrieving surface temperature [97, 98].

In summary, ARTS has been used for a wide range of applications. The vast majority are remote sensing applications, with atmospheric energetics picking up in recent years. Applications with and without scattering are almost equally frequent, with a slight majority for clear-sky. A big majority of applications is passive, but radar also plays a certain role [60,62,69].

In terms of frequency region, microwave to sub-mm applications were most common, terahertz and infrared applications were less frequent, and solar applications rare (as expected). This distribution aligns well with the historical development of ARTS, which started as a microwave program and over the years expanded to higher and higher frequencies.

#### 1.4. Python integration

In order to allow the widest possible range of different absorption and radiative transfer simulations, ARTS uses the concept of workspace variables (which hold quantities of interest, such as a vector of simulation frequencies) and workspace methods (which operate on the workspace variables to for example calculate absorption). In the past, calculations were specified in ARTS' own – quite primitive – scripting language. This is still possible, but for most users it will be much more convenient to use pyarts, the new Python interface to these workspace variables and methods, and thus specify the calculation in the form of a Python script.

It is worth pointing out here, that pyarts and ARTS really are the same program. Pyarts just is the name of the Python module. The C++ header library pybind11 [99] is used to automatically generate Python interfaces to the C++ workspace methods. So, pyarts is not ARTS translated to Python, but a python interface to the C++ ARTS methods, and the ARTS workspace.

To work with ARTS in Python, the user has to import module pyarts and create an object of type Workspace. Workspace variables and methods are simply member variables and member functions of that object.

Just enter the name of a workspace variable in an interactive Python session to see its content, or use Python's print() function. In some cases, you may have to append '.value' after the variable name to access its contents. In the ipython shell, type a question mark at the end of a workspace method or variable name to see its built-in documentation. You can also find it online on the ARTS homepage.

An overall design goal for pyarts was that it should feel 'pythonic' — natural for any user familiar with other python packages. Pyarts allows all computations that the traditional interface allowed, but with much greater convenience and flexibility. We therefore recommend to use this new interface, even though the old one is still maintained for now (it may be phased out at some point in the future). To ease the transition, we provide also a simple method that parses traditional ARTS controlfiles and translates them into python.

To convey a flavor of how it is to use pyarts, Table 3 gives a complete code example, which computes the absorption cross section spectrum of water vapor and displays it in a simple plot, shown in Fig. 1.

In Code Section 1, it is made sure that the ARTS spectral line catalog is available (if not, it is downloaded automatically), and then the ARTS workspace object is created.

Code Section 2 deals with specifying the absorption species to consider, in this case the line-by-line spectrum of water vapor according to the ARTS catalog (based on HITRAN), and the MT\_CKD 4.0 self- and foreign continuum of water vapor [100]. It also sets the correct cutoff to the lineshape function for the line spectrum, which is very important in order to get correct total absorption when the continuum models are used. (This procedure is explained in numerous articles, for example in the historical overview by Shine [101].) Note that ARTS uses SI base units throughout, so the canonical cutoff value of  $25\text{ cm}^{-1}$  becomes  $750\text{e9 Hz}$ . All function calls in this code section are calls of ARTS workspace methods (which have detailed descriptions in the ARTS online documentation).

Code Section 3 sets up how to actually compute the absorption. The workspace method propmat\_clearsky\_agendaAuto, which is new in this ARTS release, is very convenient for this. It creates an agenda with just the right workspace methods for the task, based on the selection of absorption species in the workspace variable abs\_species, which was set in the previous code section.

Code Section 4 deals with some workspace variables that are needed for advanced features, such as the magnetic field, which is used for calculations with Zeeman splitting. Here we just set them all to empty, because we do not want to use them in this calculation.

Code Section 5 defines the input quantities for our calculation, that is, pressure, temperature, the volume mixing ratio of water vapor, and also the frequency grid. The latter is set first in wavenumber units (Kayser) then converted to the ARTS internal SI base unit of Hz. This is a nice example illustrating the convenience of using python as the control language: The conversion is done by a lower level helper function, not a workspace method, that is also exposed to Python by pybind11. Note that one could also simply program the conversion, or any other transformations that one might want to apply, in Python directly.

Code Section 6, finally, does the actual calculation. The agenda that was built automatically in Code Section 3 is executed, and it stores its results in the workspace variable for the propagation matrix  $\mathbf{K}$ , called propmat\_clearsky (more on  $\mathbf{K}$  in the next section).

In this case, because the workspace variable stokes\_dim was set to 1 in Code Section 4,  $\mathbf{K}$  contains only a single element (see Eq. (4)), corresponding to the extinction coefficient (here identical to the absorption coefficient, since there is no scattering).

We then extract that value, convert it from an absorption coefficient to an absorption cross section, and store it in the variable xsec. For the unit conversion, we divide by the product of volume mixing ratio and total number density (which we compute from pressure and temperature using the ideal gas equation). Normal Python functionality comes handy for this transformation also. A factor  $10^4$  comes from the conversion from  $\text{m}^2$  (SI base unit) to the more conventional  $\text{cm}^2$  that we use for plotting.

In Code Section 7, all that is left to do is to create the line plot that is displayed in Fig. 1, using Python's powerful matplotlib module.

Hopefully, this quite explicit example helps to convey a feeling for what can be done with this new radiative transfer tool, by freely mixing the specialized ARTS functions with general python code. For more examples see the ARTS online documentation, in particular 'getting started' there. The location is given in Section 'Obtaining ARTS' at the end of this article.

## 2. Radiative transfer

### 2.1. Theory

The core equation for ARTS' internal radiative transfer solver is the vector Schwarzschild equation

$$\frac{d\vec{I}}{ds} = -\mathbf{K}(\vec{I} - \vec{J}) \quad (1)$$

**Table 3**

Python example to compute and display the absorption cross section of water vapor.

```

1 import matplotlib.pyplot as plt
2 import numpy as np
3 import pyarts
4
5 # 1) Prepare ARTS workspace
6 pyarts.cat.download.retrieve() # Download ARTS catalogs and set search path
7 ws = pyarts.workspace.Workspace() # Initialize ARTS
8
9 # 2) Set up absorption species and read catalog data
10 ws.abs_speciesSet(species=["H2O, H2O-SelfContCKDMT400, H2O-
    ForeignContCKDMT400"])
11 ws.ReadXML(ws.predefined_model_data, "model/mt_ckd_4.0/H2O.xml")
12 ws.abs_lines_per_speciesReadSpeciesSplitCatalog(basename="lines/")
13 ws.abs_lines_per_speciesCutoff(option="ByLine", value=750e9)
14
15 # 3) Set up line-by-line calculation
16 ws.lbl_checkedCalc() # Check that the line-by-line data is consistent
17 ws.propmat_clearsky_agendaAuto() # Set up propagation matrix calculation
18
19 # 4) Initialize required workspace variables
20 ws.stokes_dim = 1 # Unpolarized
21 ws.jacobian_quantities = [] # No derivatives
22 ws.select_abs_species = [] # All species
23 ws.rtp_mag = [] # No magnetic field
24 ws.rtp_los = [] # No particular LOS
25 ws.rtp_nlte = pyarts.arts.EnergyLevelMap() # No NLTE
26
27 # 5) Set up the frequency grid and the atmospheric conditions
28 f_grid_kayser = np.linspace(10, 2400, 30000) # Frequency grid in Kayser
29 ws.f_grid = pyarts.arts.convert.kaycm2freq(f_grid_kayser) # Convert to Hz
30 ws.rtp_pressure = 1000e2 # 1000 hPa
31 ws.rtp_temperature = 295 # At room temperature
32 ws.rtp_vmr = [0.02] # H2O VMR
33
34 # 6) Calculate the absorption cross section
35 ws.AgendaExecute(a=ws.propmat_clearsky_agenda) # Call the agenda
36 xsec = ws.propmat_clearsky.value.data.flatten() / (
37     ws.rtp_vmr.value[0] * ws.rtp_pressure.value
38     / (pyarts.arts.constants.k * ws.rtp_temperature.value)
39 ) * 10000 # Convert absorption coefficients to cross sections in cm^2
40
41 # 7) Plot the absorption of this example
42 fig, ax = plt.subplots(figsize=(8, 4))
43 ax.semilogy(f_grid_kayser, xsec, lw=0.2, alpha=0.5, color="#932667")
44 def rolling_mean(x, w=1000):
45     return np.convolve(x, np.ones(w) / w, "valid")
46 ax.semilogy(rolling_mean(f_grid_kayser), 10 ** rolling_mean(np.log10(xsec)),
47     lw=2, color="#932667")
48 ax.set_xlabel("Wavenumber / cm$^{-1}$")
49 ax.set_ylabel("Absorption cross section / cm$^2$ molecule$^{-1}$")
50 ax.set_xlim(f_grid_kayser.min(), f_grid_kayser.max())
51 ax.spines[["right", "top"]].set_visible(False)
52 fig.savefig("h2o-xsec.pdf")
53 plt.show()

```

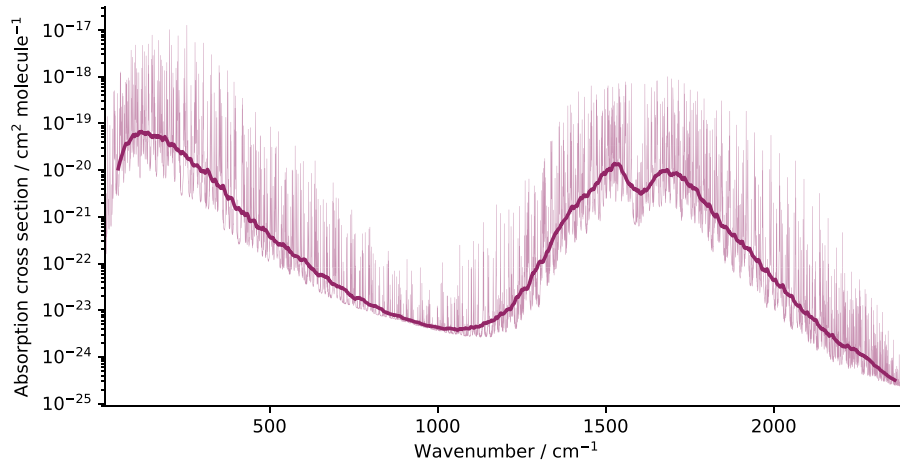


**Fig. 1.** Absorption cross section of water vapor computed with the Python code in Table 3. The heavy line is a geometric running mean (averaging logarithmic values consistently with the plot's logarithmic scale).

where  $\vec{I}$  is the four component Stokes vector,  $\vec{J}$  is the source term, and  $\mathbf{K}$  is the propagation matrix, which describes how the radiation is modified along an infinitesimal path distance  $ds$ .

The equation formally looks exactly as the original scalar Schwarzschild equation [102], but has a wider scope, not only because  $\mathbf{K}$  is a matrix and  $\vec{I}$  and  $\vec{J}$  are vectors, but also because  $\mathbf{K}$  and  $\vec{J}$

include the effect of scattering, whereas Schwarzschild thought only about absorption and thermal emission. The advantage of casting the radiative transfer differential equation in this form is that its integral form is known.

One key implementation difference of ARTS version 2.6 compared to version 2.2 is that it now uses a dedicated data type for the propagation matrix  $\mathbf{K}$ , which greatly speeds up the calculation of polarized radiative transfer by simplifying both matrix inversions and matrix exponential calculations.

We assume in ARTS and in this subsection that  $\mathbf{K}$  and  $\vec{J}$  are approximately constant over a small enough distance  $r = |s_{i+1} - s_i|$ , where  $i$  is some discrete positional index. In fact, we discretize ARTS in a level-by-level manner and both  $\mathbf{K}$  and  $\vec{J}$  are simply the average of the surrounding levels when a layer is constructed, explicitly,  $\mathbf{K} = (\mathbf{K}_i + \mathbf{K}_{i+1})/2$  and  $\vec{J} = (\vec{J}_i + \vec{J}_{i+1})/2$ . Given this, the transmission through the atmosphere between two positions can be written as

$$\vec{I}_{i+1} = \exp(-\mathbf{K}r) \vec{I}_i \quad (2)$$

when the source term is negligibly small, or

$$\vec{I}_{i+1} = \exp(-\mathbf{K}r) (\vec{I}_i - \vec{J}) + \vec{J} \quad (3)$$

when the source term must be taken into account.

The propagation matrix has in other places been called the extinction matrix or the attenuation matrix. We prefer the term propagation matrix, because this matrix also deals with the effect of Faraday rotation, which just moves energy between different polarization states (higher Stokes components), but does not decrease the total intensity (first Stokes component), so that  $\mathbf{K}$  is not always associated with extinction. The physical unit of  $\mathbf{K}$  is  $\text{m}^{-1}$ .

There are only 7 independent variables in the  $4 \times 4$  propagation matrix

$$\mathbf{K} = \begin{bmatrix} A & B & C & D \\ B & A & U & V \\ C & -U & A & W \\ D & -V & -W & A \end{bmatrix}, \quad (4)$$

so only these are kept. The Zeeman effect uses all seven components, Faraday rotation only uses the  $U$ -component, and all the other line-by-line, continua, and collision-induced-absorption models of ARTS only use the  $A$ -component, corresponding to the scalar extinction coefficient for unpolarized radiation, which would be the sum of absorption coefficient and scattering coefficient.

The matrix exponential  $\exp(-\mathbf{K}r)$  is computed after a rewrite as

$$\exp(-Ar) \exp(\mathbf{K}'), \quad (5)$$

where  $\mathbf{K}'$  is as Eq. (4) but with  $A = 0$  and scaled already by  $r$  (this is the same solution as found in [103]). We can rewrite the remaining matrix exponential using the Cayley–Hamilton theorem as

$$\exp(\mathbf{K}') = c_0 \mathbf{I} + c_1 \mathbf{K}' + c_2 \mathbf{K}'^2 + c_3 \mathbf{K}'^3, \quad (6)$$

where  $c_0$ – $c_3$  are four coefficients that can be found using eigenvalue decomposition. The eigenvalues ( $\lambda$ ) are found from solving the characteristic polynomial,

$$\begin{aligned} 0 &= \lambda^4 + b\lambda^2 + c \\ b &= U^2 + V^2 + W^2 - B^2 - C^2 - D^2 \\ c &= -(DU - CV + BW)^2 \\ s &= \sqrt{b^2 - 4c} \\ x^2 &= \sqrt{\frac{s-b}{2}} \\ y^2 &= \sqrt{\frac{s+b}{2}}, \end{aligned} \quad (7)$$

where  $x^2$  and  $y^2$  are the positive and negative parts of the solutions for  $\lambda^2$ , respectively, as their practical real values. The coefficients of Eq.

(6) are found from the set of equations

$$\begin{aligned} e^x &= c_0 + c_1 x + c_2 x^2 + c_3 x^3 \\ e^{-x} &= c_0 - c_1 x + c_2 x^2 - c_3 x^3 \\ e^{iy} &= c_0 + ic_1 y - c_2 y^2 - ic_3 y^3 \\ e^{-iy} &= c_0 - ic_1 y - c_2 y^2 + ic_3 y^3, \end{aligned} \quad (8)$$

which yields

$$c_0 = \frac{x^2 \cos y + y^2 \cosh x}{x^2 + y^2} \quad (9)$$

$$c_1 = \frac{x^2 \frac{\sin y}{y} + y^2 \frac{\sinh x}{x}}{x^2 + y^2} \quad (10)$$

$$c_2 = \frac{\cosh x - \cos y}{x^2 + y^2} \quad (11)$$

$$c_3 = \frac{\frac{\sinh x}{x} - \frac{\sin y}{y}}{x^2 + y^2}. \quad (12)$$

Lastly, it is important to keep some limits in mind as  $x \rightarrow 0$  or  $y \rightarrow 0$  as the hyperbolic and the trigonometric functions are not computationally stable while they are divided by some numbers close to 0. For convenience, these limits are

$$\begin{aligned} c_0 : \quad \lim_{x \rightarrow 0} c_0 &= \lim_{y \rightarrow 0} c_0 = 1 \\ c_1 : \quad \lim_{x \rightarrow 0} c_1 &= \lim_{y \rightarrow 0} c_1 = 1 \\ c_2 : \quad \lim_{x \wedge y \rightarrow 0} c_2 &= \frac{1}{2} \\ c_3 : \quad \lim_{x \wedge y \rightarrow 0} c_3 &= \frac{1}{6} \\ \lim_{x \rightarrow 0} c_3 &= \frac{1}{y^2} - \frac{\sin y}{y^3} \\ \lim_{y \rightarrow 0} c_3 &= \frac{\sinh x}{x^3} - \frac{1}{x^2}, \end{aligned} \quad (13)$$

where  $x \wedge y \rightarrow 0$  means that both variables approach zero. We have opted for a value of 0.001 as a limit of actual 0 of  $x$  and  $y$ .

As a comment on the numerics of this matrix exponential solution, we are not sure how stable the method really is, but it is very fast. The work by Moler and Van Loan [104] gives the scaling and squaring method with the Padé approximation as one of the most effective algorithms at hand. The algorithm above is more than an order of magnitude faster in our experience.

The differences between the methods in computed results are small if the maximum value in  $\mathbf{K}'$  is small (less than 0.1) but grow out of control if this is large (above 10). We cannot judge which method is then better, but we do note that the Padé approximation algorithm tends to return infinities when the algorithm above still returns large but finite values. In any case, since an atmospheric layer with too much absorption is a poorly designed atmospheric layer, for the sake of radiative transfer using the faster algorithm above is simply better.

The source function is first computed as

$$\vec{J} = \mathbf{K}^{-1} (\vec{\alpha} B_p + \vec{J}_n + \vec{J}_s + \vec{J}_\odot), \quad (14)$$

where  $\vec{\alpha} = \{A, B, C, D\}^T$  is the absorption vector,  $B_p$  is Planck's function,  $\vec{J}_n$  is the emission correction due to non-local thermodynamic equilibrium,  $\vec{J}_s$  is the additional particulate scattering source term, and  $\vec{J}_\odot$  is the additional solar scattering term.

When the atmosphere is in local thermodynamic equilibrium, and there is no Sun, and scattering is not considered, this simply translates to  $\vec{J} = \{B_p, 0, 0, 0\}^T$ . This can be seen from noting that  $\mathbf{K}^{-1} \mathbf{K}$  is the unit matrix and  $\vec{\alpha}$  is just the first column of  $\mathbf{K}$ . The  $\vec{J}_n$  is computed as the additional emission caused by non-local thermodynamic equilibrium added up for every absorption species. Note also that the split above is done mostly for pedagogical reasons. Inside ARTS  $\vec{J}_n$  and  $\vec{J}_s$  are treated as the same variable, but  $\vec{J}_\odot$  is still treated separately.

The background source term,  $\vec{I}_0$ , depends on the background of the propagation path. Three such backgrounds are allowed: (1) surface, (2) space, and (3) a cloud box. The surface in particular might itself recursively spawn a new set of radiative transfer calculations to

compute the incoming radiation. For propagation paths with space as background, the sun is added as background source if the propagation path in reverse direction hits the solar disc. This allows to resolve the shape of the sun or to track the sun through the atmosphere.

## 2.2. Simulations with a solar source term

In this subsection we will give a brief overview about simulations with a solar source. There will be also an upcoming article dedicated to this. The simulation of solar radiation in ARTS is based on the assumption that the distance between the Sun and any position within the atmosphere or on the surface is much larger than the radius of the Sun. This means that the angular variability of radiation leaving the surface of the Sun can be neglected and the incoming spectral radiance is assumed to be parallel (collimated beam approximation, [105]). For a position at the top of the atmosphere (TOA), the incoming spectral radiance (in units of  $\text{W m}^{-2} \text{sr}^{-1} \text{Hz}^{-1}$ ) in direction  $\Omega$  at TOA can be described as

$$I_{s,TOA}(\Omega) = F_{s,TOA} \delta(\Omega - \Omega') \quad (15)$$

with  $\Omega'$  the direction from the center of the Sun to TOA and  $F_{s,TOA}$  the spectral irradiance (in units of  $\text{W m}^{-2} \text{Hz}^{-1}$ ) at TOA and  $\delta$  the Dirac function. The spectral irradiance  $F_{s,TOA}$  at TOA is

$$\begin{aligned} F_{s,TOA} &= \int_0^{2\pi} \int_0^{\alpha_{s,TOA}} I_s \cos \theta \sin \theta d\theta d\phi \\ &= \pi I_s \sin^2 \alpha_{s,TOA} \\ &= F_s \sin^2 \alpha_{s,TOA}, \end{aligned} \quad (16)$$

with  $\alpha_{s,TOA}$  the solar angular radius at TOA,  $F_s$  the solar spectral irradiance at the position of the Sun in space and  $I_s$  the hemispherically isotropic radiance leaving the surface of the Sun. The factor  $\sin^2 \alpha_{s,TOA}$  takes into account that the irradiance is changing with the inverse square of the distance as it is

$$\sin^2 \alpha_{s,TOA} = \frac{r_s^2}{d_{s,TOA}^2 + r_s^2} \quad (17)$$

with  $r_s$  the radius of the sun and  $d_{s,TOA}$  the distance between TOA and the center of the sun. Inserting (16) in (15) results in

$$I_{s,TOA}(\Omega) = F_s \sin^2 \alpha_{s,TOA} \delta(\Omega - \Omega') \quad (18)$$

This approach makes it possible to use the same solar spectrum for different distances of the sun, for example to simulate radiation for different planets or different orbital configurations. The only thing, that needs to be changed is the actual distance between the sun and the planet. The incoming spectral radiance is automatically adjusted. Note that  $F_s$  is formally defined at the center of the sun, although it could of course never be observed there. At the surface of the sun  $I_s$  is already reduced by a factor of 1/2, according to Eq. (17).

ARTS assumes an elliptical geometry. This has some implications compared to a plane parallel geometry. For example, the distance between the sun and TOA is not unique but depend on the geographical position. In Fig. 2 the distance  $R_A$  at TOA location A is greater than the distance  $R_B$  at TOA location B. This also results in different angular radii, because the angular radius  $\alpha_s$  depends on the distance. The resulting differences due to the different geographical positions are small, in the order of  $0.1 \text{ W m}^{-2}$ , but they can be important for reference simulations, especially when comparing to simulations with other geometries. Furthermore, the direction  $\Omega'$  from the sun to TOA depends on the geographical position because the radiative transfer is relative to a local coordinate system. For example, the local solar incidence angles  $\theta_A$  and  $\theta_B$  in Fig. 2 differ, which results in different directions  $\Omega'$ .

In addition to the irradiance spectrum, a solar source is defined by the radius of the Sun, its distance to the planet and the geographical position where the Sun is at zenith on the planet. A solar spectrum can

**Table 4**

Summary of available line shape operators in ARTS and their input parameters.  $G_D$  is the Doppler width,  $G_0$  is the speed-independent pressure width,  $D_0$  is the speed-independent pressure frequency shift,  $G_2$  is the speed-dependent pressure width,  $D_2$  is the speed-dependent pressure frequency shift,  $f_c$  is the frequency of velocity changing collisions, and  $\eta$  a correlation factor. Except for  $G_D$ , the other parameters depend on temperature as detailed in Table 5. See Tran et al. [109] for details, we follow them in our definitions.

Line shape	Parameters
Doppler	$G_D$
Lorentz	$G_0, D_0$
Voigt	$G_D, G_0, D_0$
Speed-dependent Voigt	$G_D, G_0, D_0, G_2, D_2$
Hartmann-Tran	$G_D, G_0, D_0, G_2, D_2, f_c, \eta$

be defined as a black body with an effective emission temperature or as an arbitrary user-defined spectrum.

There are two solvers in ARTS capable of simulations with a solar source term: First, there is ARTS' internal clear-sky solver iyClearsky. It is a 3D fully polarized radiative transfer solver for spherical geometry. It includes first order molecular scattering from solar sources but no scattering of particulates or scattering from thermal sources.

Second, there is CDISORT [106], which is DISORT 2.1 [105] ported to C and for simplicity called DISORT from here on. It is a 1D non-polarized radiative transfer solver for plane parallel atmospheres and can handle multiple scattering. In contrast to iyClearsky, DISORT can have only one solar source. As DISORT is a plane parallel solver and ARTS assumes a spherical geometry, it needs to be run for a specific geographic position because the local solar zenith angle, which DISORT internally needs, is calculated from the specific geographic position and the geographic zenith position of the Sun.

For both solvers molecular scattering (Rayleigh scattering) is provided by a parametrization from M. Callan, University of Colorado [105] based on the results of Bates [107] for the scattering cross sections and the Rayleigh phase matrix including depolarization from Hansen et al. [108].

## 3. Absorption

### 3.1. Computing absorption from spectroscopic data

How ARTS computes absorption coefficients by summing up spectral lines based on spectroscopic data has been completely re-implemented. The set of operators and multiplications for each spectral line is

$$\alpha = (1 + G_{lm} - iY_{lm}) S(T, p, \dots) N(\nu, \dots) F(\nu, \dots), \quad (19)$$

where  $\alpha$  is the complex absorption coefficient, whose real part is the attenuation and imaginary part is the dispersion. The  $G_{lm}$  and  $Y_{lm}$  parameters are the second and first order line mixing coefficients, the  $S$  operator computes the line strength, the  $N$  operator renormalizes the line shape, and the  $F$  operator computes the line shape. Furthermore,  $i$  is the imaginary unit,  $T$  is temperature,  $p$  is pressure, and  $\nu$  is frequency.

There are many variants and combinations of these operators available. For the line shape  $F$ , Table 4 gives a summary of available operators and what user input they depend on, and Table 5 lists what temperature dependence models for these parameters are supported.

As one example, the adaptation of default HITRAN line-by-line data for ARTS [24] uses

$$\alpha = \frac{x_s p}{kT} S_i \frac{Q(T_0)}{Q(T)} \exp\left(E_i \frac{T - T_0}{kT T_0}\right) \frac{\nu (\exp[h\nu/kT] - 1)}{\nu_i (\exp[h\nu_i/kT_0] - 1)} F_\nu(\dots), \quad (20)$$

where the terms before the  $F_\nu(\dots)$  line profile operator represent the  $S$  and  $N$  operations of Eq. (19),  $x_s$  is the volume mixing ratio of the molecule in question,  $k$  is Boltzmann's constant,  $S_i$  is the reference

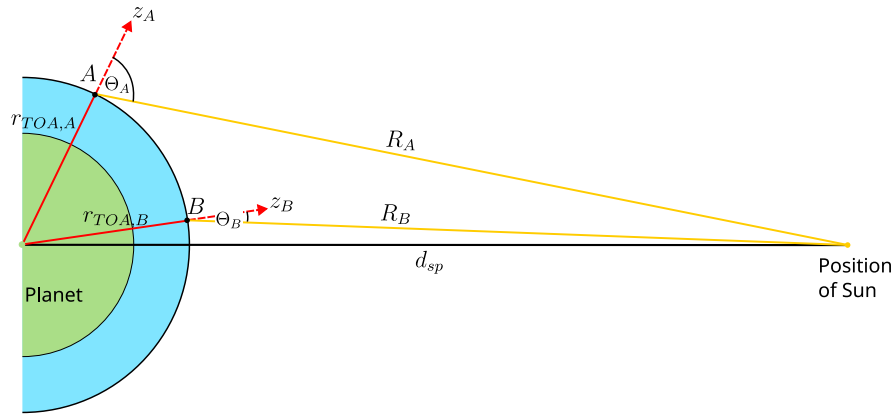


Fig. 2. Sketch of the sun planet geometry.  $R_A$  and  $R_B$  are the distance from the TOA locations A and B to the sun.  $r_{TOA,A}$  and  $r_{TOA,B}$  are the distance between the center of the planet and the TOA locations A and B.  $z_A$  and  $z_B$  define the local vertical directions and  $d_{sp}$  is the distance between the position of the Sun and the center of the planet.

Table 5

Temperature dependence of line shape parameters in Table 4. The names are as enumerated inside ARTS. The coefficients that are provided by the user are  $X_0$ ,  $X_1$ ,  $X_2$ , and  $X_3$ .  $T$  is the current temperature and  $T_0$  is the reference temperature.

Model	Formulation
T0	$X_0$
T1	$X_0 \left(\frac{T}{T_0}\right)^{X_1}$
T2	$X_0 \left(\frac{T}{T_0}\right)^{X_1} \left[1 + X_2 \log\left(\frac{T}{T_0}\right)\right]$
T3	$X_0 + X_1(T - T_0)$
T4	$\left[X_0 + X_1 \left(\frac{T}{T_0} - 1\right)\right] \left(\frac{T}{T_0}\right)^{X_2}$
T5	$X_0 \left(\frac{T}{T_0}\right)^{0.25+1.5X_1}$
AER	$X(T = 200) = X_0$ , $X(T = 250) = X_1$ , $X(T = 296) = X_2$ , $X(T = 340) = X_3$ , linear interpolation
DPL	$X_0 \left(\frac{T}{T_0}\right)^{X_1} + X_2 \left(\frac{T}{T_0}\right)^{X_3}$
POLY	$X_0 + X_1 T + X_2 T^2 + X_3 T^3$

line strength of the absorption line as provided by HITRAN,  $Q$  is the total internal partition sum operator for some temperature [110],  $T_0$  is the reference temperature of the line (for HITRAN always 296 K),  $E_i$  is the HITRAN lower state energy level of the absorption line,  $\nu$  is the frequency at which absorption is sampled,  $\nu_i$  is the HITRAN reference line center of the absorption line, and  $h$  is the Planck constant. HITRAN does not provide any line mixing parameters by default, so the  $1 + G_{lm} - iY_{lm}$  term of Eq. (19) disappears completely.

The  $F_\nu(\dots)$  line profile operator in this example case is

$$F_\nu(\dots) = \frac{1}{\sqrt{\pi}G_D} w\left(\frac{\nu - \nu_i - D_0 + G_0}{G_D}\right) \quad (21)$$

$$G_D = \frac{\nu_i}{c} \sqrt{\frac{2000RT}{m_s}} \quad (22)$$

$$G_0 = x_s \gamma_{i,s} p \left(\frac{T_0}{T}\right)^{n_{i,a}} + (1 - x_s) \gamma_{i,a} p \left(\frac{T_0}{T}\right)^{n_{i,a}} \quad (23)$$

$$D_0 = \delta \nu_{i,a} p \quad (24)$$

where  $w$  is the Faddeeva function (the convolution of the Doppler line profile and the Lorentz line profile [111]),  $c$  is the speed of light,  $m_s$  is the molar mass of the molecule in question,  $R$  is the universal gas constant,  $\gamma_{i,s}$  is the HITRAN self broadening coefficient,  $\gamma_{i,a}$  is the HITRAN air broadening coefficient,  $n_{i,a}$  is the HITRAN air broadening temperature exponent, and  $\delta \nu_{i,a}$  is the HITRAN air pressure shift. In Eq. (22), a factor 1000 comes in because we give the molar mass  $m_s$  in grams per mole, and  $R$  and  $T$  in SI units (as all other quantities).

Comparing the expressions of Eqs. (21) to (24) to Tables 4 and 5 shows that with the standard HITRAN data we are using a Voigt line shape with the T1 temperature model for the parameters going into the pressure width  $G_0$  and the T0 temperature model for the parameter going into the pressure shift  $D_0$ .

By default, HITRAN does not provide the more complete Hartmann-Tran profile parameters [109], but ARTS can in principle compute the Hartmann-Tran profile if the parameters are supplied. For this the users must provide the parameters listed in the last row of Table 4 in a form fitting on of the temperature models of Table 5 and set the appropriate line profile operator.

One additional complication not covered by any of the expressions above occurs when the atmosphere is considered in non-local thermodynamic equilibrium as this will contribute to the  $\tilde{J}_n$  term of Eq. (14). Yamada et al. [112] describes the basics of the implementation in ARTS to compute non-local thermodynamic equilibrium.

### 3.2. Other absorption

Besides spectral line by spectral line absorption calculations, ARTS also includes state of the art absorption continua, such as CKD\_MT up to Version 4 for water vapor (from Version 4 on CKD\_MT water vapor continuum coefficients are stored as external data and distributed via the HITRAN website, so any later version will also work). Furthermore, HITRAN collision-induced absorption ([113], last HITRAN data access July 2022) and absorption cross section data [19] are also available, for example for halocarbons as described in [20]. Continua and other absorption functions will continue to be updated as new data become available.

## 4. Scattering

This section deals with simulations where scattering by particles within the atmosphere is considered. Particles here refers to hydrometeors (liquid or frozen cloud and precipitation particles) or aerosols. ARTS 2.6 handles for the first time also molecular scattering (for UV/visible radiation) but this is to be described in another article. This section starts by outlining the input data required, and ends with an overview of available scattering solvers.

### 4.1. Particle properties

The combination of shapes and sizes of aerosols and hydrometeors is basically unlimited and, as a consequence, the core manner in ARTS to describe particle properties is generic by design. It is up to the user to decide what set of scattering elements to include in the calculations. The definition of a scattering element has two parts, the single scattering properties of the element and the associated number density.

#### 4.1.1. Single scattering data

ARTS has its own format for single scattering data. These data represent the extinction, absorption and scattering function, gridded as a function of frequency and temperature, of the scattering element. For a limited set of shapes, including spheroids and cylinders, the single scattering data can be calculated with a relatively low calculation burden by the T-matrix method. ARTS contains an interface to such code, the one by [114]. For more complex shapes, the scattering data have to be calculated externally. For hydrometeors and calculations at frequencies between 1 and 900 GHz, the ARTS infrastructure contains an extensive database of precomputed values. This ARTS single scattering database consists of two parts. The broadest selection of habits (i.e., shape model) is offered for the standard assumption of totally random orientation (TRO), for details see [17]. The ARTS format can also represent particles that just have azimuthally random orientation (ARO). The corresponding part of the database contains data for two habits [18]. Data from other databases covering cloud ice particles have been converted to the ARTS format and been applied. We are not aware of any application of ARTS involving scattering by aerosols, but this should in principle also be possible.

#### 4.1.2. Particle number densities and size distributions

The user can opt to directly import particle number densities for the chosen scattering elements, if such are at hand from an external source or are calculated on the Python side. However, more common is the case that the user has bulk properties, such as condensate mass concentrations, and from this wants to generate particle number concentrations that follow a particle size distribution (PSD). To simplify this process, a number of PSD parameterizations are included in ARTS. For clarity, it should be noted that a PSD is a continuous size distribution (for example in units of  $\#/(m^3 \cdot m)$ ), while derived particle number densities are values integrated/binned in size (for example in units of  $\#/m^3$ ).

First of all, there is a set of methods for treating the PSD as a modified gamma distribution (MGD), implemented following the nomenclature and equations of [115]:

$$n(x) = N_0 x^\mu e^{-Ax^\gamma}, \quad (25)$$

where the four MGD parameters are  $N_0$ ,  $\mu$ ,  $A$ , and  $\gamma$ , and  $x$  is the measure on size. To allow analytical expressions for all needed operations, the relationship between size and mass must follow a power-law:

$$m = ax^b. \quad (26)$$

As long as Eq. (26) can be fulfilled,  $x$  can represent any selection of size. For example, to let  $x$  represent mass, both  $a$  and  $b$  have to be set to 1. See [115] for further choices.

The MGD methods allow that  $N_0$ ,  $\mu$ ,  $A$  and  $\gamma$  all vary throughout the atmosphere, but can also be set to be constant. That is, the user can operate with up to four moments. There are methods for expressing one moment as bulk mass [ $kg/m^3$ ], possibly combined with a second bulk property. This second moment can be number density, mean particle mass, mean size or median size. There is also a MGD method handling the common assumption of a power-law relationship between  $N_0$  and  $A$ . The generic PSD methods include also two methods for setting up mono-dispersive distributions.

There are several PSD methods specific for hydrometeors. For rain the PSDs of [116,117] are included. The classical rain PSD of [118] is covered by the general MGD methods. For ice hydrometeors, the parameterizations of [119–122] are included. Also included are two PSD schemes matching multimoment microphysics schemes common in atmospheric models [123,124].

All these methods can provide the derivative of the PSD with respect to free parameters (that is, the moments used). This is a prerequisite to perform OEM inversions of observations involving scattering. However, just two of the scattering solvers can actually use this feature, see below.

#### 4.2. Scattering solvers

Algorithms performing radiative transfer in the presence of scattering are referred to as scattering solvers. Common to these algorithms is that they solve the problem that, due to scattering, radiation traveling in a given direction depends on the radiation in all other directions at the same point. Expressed in the mathematics of Section 2.1, the computation of the  $\bar{J}_s$  term in Eq. (14) would require an integral over the radiation Stokes vector  $\bar{I}$  from all incoming directions, weighted by the scattering phase matrix, making the simple solution of integrating along a single line of sight, as in Eq. (3), impossible.

Different scattering solvers employ different strategies to overcome this. In doing so, they use their own internal representation of the radiation field, and their own intrinsic approximations and simplifications, such as scalar (unpolarized) radiation only, one-dimensional atmospheres, and often plane-parallel geometry. It goes beyond the scope of this text to discuss the different solver strategies, good overviews are given for example in [125–128]. Instead, the goal here is to describe the solvers that are available in ARTS, along with their strengths and limitations, where limitations include those that are intrinsic to the solver and those related to our implementation or the coupling to ARTS.

ARTS comes with two types of scattering solvers, a set for calculating scattering of thermal emission, resulting in radiances, and two methods for simulating radar reflectivity measurements. These are described in separate subsections below.

##### 4.2.1. Radiances

The discrete ordinate iterative (DOIT) [2] and the Monte Carlo (MC) [6] solvers were developed directly for ARTS and were introduced by [12]. More recently, interfaces to two external scattering solvers have been added, namely DISORT and RT4. The MC module is restricted to simulate remote sensing observations, while DISORT, DOIT and RT4 provide the full radiance field and can thus also form the basis for flux calculations (Section 5). Table 6 gives a summary of the scattering solvers covered by this section and their individual limitations.

The DISORT approach [129] is arguably the most established scattering solver in our field and exists in several implementations. ARTS is coupled to the code of [106]. In contrast to other scattering solvers in ARTS, DISORT is limited to unpolarized (scalar) calculations and thus also to totally random particle orientation (TRO).

The RT4 solver [130] fits better with the general functionality of ARTS. It handles polarized radiation and scattering data for both TRO and ARO and it can be coupled to ARTS own description of specularly reflecting surfaces. A limitation of RT4 compared to DISORT is that scaling with respect to the forward scattering peak is missing. RT4 also cannot yet be used with multi-threading inside ARTS, mainly as RT4 comes as FORTRAN code.

Both DISORT and RT4 assume a plane-parallel atmosphere (in other words an infinite planet radius), while remaining parts of ARTS operate with a spheroidal reference geoid. Another deviation to ARTS is that RT4 and DISORT take layer-means as input, while ARTS operates with point values (assuming a linear variation, in each spatial dimension, between grid points). To overcome this difference, an averaging is performed between the altitude levels of ARTS. That is, if the ARTS pressure grid has  $n$  points, DISORT and RT4 will be used with  $n-1$  layers. This difference in discretization can be significant if comparing radiances between scattering solvers inside ARTS.

To extend the usage of the scattering solvers of 1D character, an independent beam approximation (IBA) wrapper method has been implemented. This method allows to apply the 1D solvers in simulations of remote sensing data done using 2D and 3D atmospheres. The IBA strategy is to calculate the propagation path through the 2D or 3D atmosphere, and interpolate the atmospheric and surface fields to the points of the path. After the interpolation, the obtained values are used to create a, likely slanted, 1D view of the atmosphere. The final

**Table 6**

ARTS radiance scattering solvers. The columns are, starting from left: short name of the solver, if vector (polarized) radiative transfer can be made, if 3D geometry covered, if plane parallel, if suitable for flux calculations, and notable limitation or feature. Solvers having Yes below Vector can also handle particle orientation (ARO). Comments refer to the implementation in ARTS, and should not be taken as generally true in the case of third party solvers.

Name	Vector	3D	PP	Flux	Comment
DISORT	No	No	Yes	Yes	Only Lambertian surface
DOIT	Yes	Yes	No	Yes	3D not recommended
Hybrid	No	Yes	No	No	Can be used with OEM
MC	Yes	Yes	No	No	Choice for detailed 3D
RT4	Yes	No	Yes	Yes	No multi-threading

radiances for the simulation are obtained by interpolating, in angles, the radiation field given by the scattering solver based on the obtained 1D view. By applying IBA repeatedly it is possible to incorporate inhomogeneities inside the footprint of microwave sensors with relatively small errors compared to full 3D MC calculations [72]. For observations resulting in that the propagation path does not cover all altitudes (such as airborne upward observations), the atmosphere is sampled vertically to cover the missing altitude range, starting from the observation point.

None of the scattering solvers mentioned above provides the Jacobian, which is a prerequisite for OEM-type retrievals (see Section 6). As a first step to overcome this limitation, a hybrid method has been implemented. In short, either DISORT, DOIT or RT4 is first run to obtain the full radiance field. The hybrid method performs an integration following Eq. (3), where the precalculated radiance field is used to calculate the scattering source term ( $\vec{J}_s$  in Eq. (14)). The general approach for deriving the Jacobian in ARTS has been extended to cover this case, but with the limitation that the incoming radiation field is assumed constant. That is, the provided Jacobian ignores the fact that a change at one point in the atmosphere can affect the scattering source term at another point. Thus the Jacobian is not fully exact, but tests showed that retrieval convergence can be achieved in most cases and the method has been applied successfully in remote sensing applications [68,69].

The hybrid method is fully integrated into ARTS. The internal functions of ARTS for performing pencil beam radiative transfer have been extended to handle a precalculated scattering source term, as required by the hybrid method. When decreasing the amount of scattering along the pencil beam, the hybrid method converges to the standard clear-sky emission solver. As an internal solver, it operates with a spherical planet. The hybrid approach calculates the radiance and the Jacobian for a specific observation direction. In this sense it is similar to the MC module, in contrast to the other, full, scattering solvers that calculate the full radiation field. Since the hybrid method needs a full radiation field as input, one should see it simply as a way to complement a solution from any of the other ARTS scattering solvers with a Jacobian.

We will end this subsection with a usage example: Fox et al. [131] used ARTS to evaluate the representation of ice clouds in a Numerical Weather Prediction (NWP) model. The Monte Carlo scattering solver was used to simulate passive sub-millimeter wave brightness temperatures from 3D NWP model input fields using ice crystal scattering properties from the ARTS database [17], and these were compared to airborne observations. The flexibility permitted by the wide range of ice crystal habits provided in the ARTS scattering database, and the different PSD parameterizations described above, make it possible to achieve good consistency between the representation of cloud microphysics in the NWP model and radiative transfer simulations.

Fig. 3 shows an example of the simulated and observed brightness temperatures between 157 and 874 GHz, and the NWP model hydrometeor fields used as input to the simulations. This example used the scattering properties of the large column aggregate particle type to represent the cloud ice. The study demonstrated that ARTS is capable of simulating realistic brightness temperatures across the full range of frequencies used, when appropriate ice crystal scattering models are selected, although in this example there are some discrepancies, particularly at 664 and 874 GHz in the vicinity of the convective core.

These are probably caused by errors in the NWP hydrometeor fields, although it is also possible that different microphysical assumptions are required in different regions of the cloud.

#### 4.2.2. Radar measurements

ARTS contains two methods for simulating atmospheric monostatic radar observations. Their complexity depends strongly on whether multiple scattering is significant or not. As a consequence, there are two distinct radar methods.

For **single scattering** only simulations, the calculation is very straightforward, and the core task is to determine the bulk backscattering and weigh it with the two-way transmission:

$$\vec{I}_b = \mathbf{T} \mathbf{Z}_b \vec{T}_i, \quad (27)$$

where  $\vec{I}_b$  is the Stokes vector for the returned radar pulse,  $\vec{I}_i$  is the unit Stokes vector describing the polarization state of the transmitted pulse,  $\mathbf{Z}_b$  is the bulk scattering matrix for the point of concern in the backscattering direction, and  $\mathbf{T}$  is the Mueller transmission matrix for the distance between the radar transmitter/receiver and the backscattering point.

The transmission matrix for the away and return directions can theoretically differ (for vector calculations, not for scalar ones), but this should be of no practical concern and is ignored here. Furthermore, the method allows to scale the extinction going into  $\mathbf{T}$ . This is a scalar value,  $r_e$ , with one as default. By setting  $r_e = 0$ , the unattenuated return pulse is obtained. At least for some situations, a full calculation with multiple scattering ends up roughly halfway between  $r_e = 0$  and  $r_e = 1$  [132], and setting  $r_e \approx 0.5$  could be considered for approximating the neglect of multiple scattering.

This single-scattering method provides the full Jacobian. That is, the Jacobian includes derivatives with respect to both  $\mathbf{Z}_b$  and  $\mathbf{T}$ . OEM retrievals using this method are found in papers by Pfreundschuh et al. [68,69].

For **multiple scattering** simulations, the calculation becomes more complex. For simulating atmospheric profiling pulse radar, the calculation of scattering events has to be considered within the context of pulse propagation time. Additionally, to avoid overestimating multiple scattering effects and properly account for the relationship between beam size and multiple scattering, simulations require a finite antenna pattern [133,134].

Following studies by Marzano et al. and Battaglia et al. [134,135], ARTS uses a Monte Carlo approach to account for multiple scattering effects from hydrometeors in the atmosphere. All scattering events have the potential to contribute to the simulated backscatter profile, so backward ray tracing would not produce any computational advantage unlike those realized for passive sensing [for example 6]. Therefore, ray tracing initiates from the transmitter using traditional forward Monte Carlo sampling.

Each discrete contribution to the radiative transfer solution is initiated by drawing two random numbers from a bivariate Normal distribution with means aligned with the sensor boresight and standard deviations related to the antenna full-width, half-maximums (FWHM) of the E- and H-planes of the antenna pattern, where  $\sigma = FWHM/2.3548$ . This procedure determines the direction of the line-of-sight for the

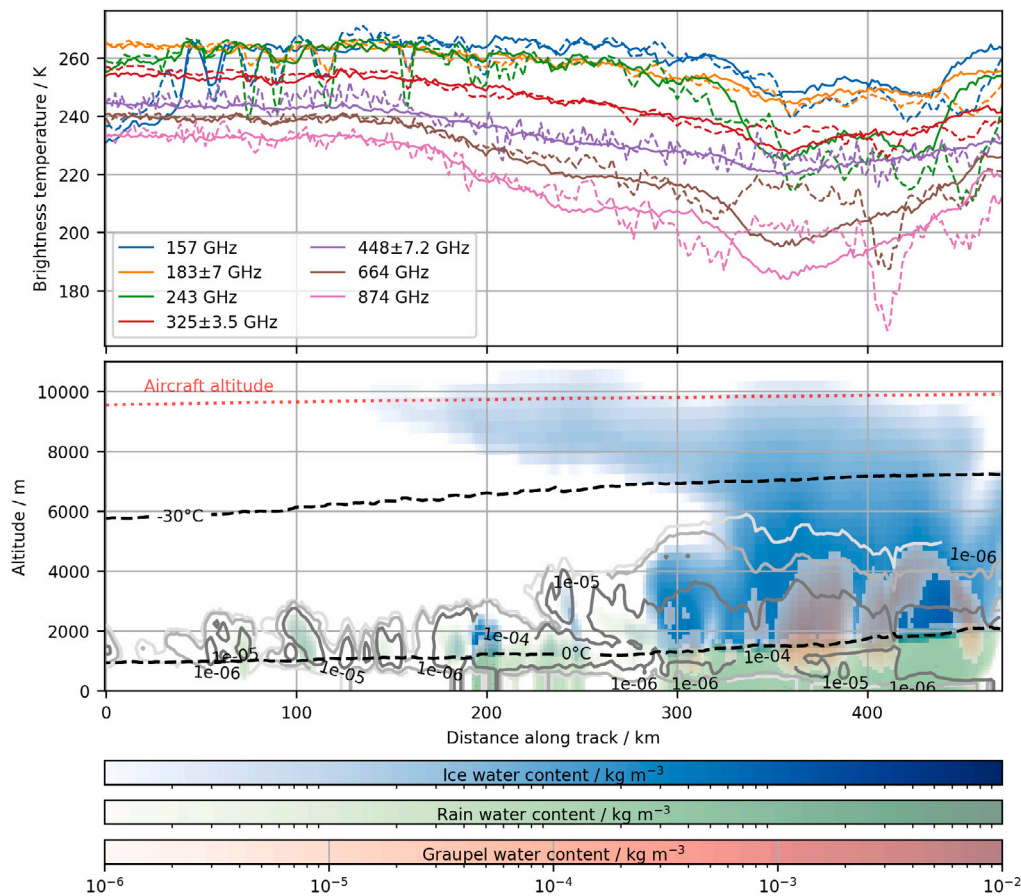


Fig. 3. Top panel: Simulated (solid lines) and observed (dashed lines) brightness temperatures between 157 and 874 GHz from a passive airborne radiometer viewing a cloudy scene. Bottom: Cross-section of the cloud fields from the NWP model used as input to the simulations. The colors represent the ice, rain and graupel water contents, and the gray contours represent the cloud liquid water content.

radiative transfer contribution under the assumption of a Gaussian antenna pattern.

Next to calculate propagation path length, a random number  $r_p$  drawn from a uniform distribution represents the scalar path transmission corresponding to the extinction of the first Stokes element  $I$ . Starting with a scalar transmission coefficient  $t_I = 1$ , the path transmission matrix is accumulated while  $t_I > r_p$ . For cases in which the bulk extinction matrix is block-diagonal due to contributions from azimuthally-random particles, transmission includes the effects on cross-polarization based on the state of the Stokes vector at the beginning of the propagation path. When  $t_I \leq r_p$ , propagation ends and the accumulated transmission matrix, and corresponding path length, are stored.

After path length and transmission calculation, the bulk scattering properties are calculated at the propagation path end. A random number  $r_a$  is drawn from a uniform distribution and compared with the single scattering albedo  $\alpha_{ss}$  (the ratio of scattering cross-section  $C_{sca}$  over extinction cross-section  $C_{ext}$ ). If  $\alpha_{ss} < r_a$ , propagation is terminated at an extinction event; otherwise, the monostatic backscatter contribution is recorded for the radar range bin corresponding to the calculated path length. This contribution includes the normalized transmission in the transmit direction, to account for polarization mixing, return transmission, and weighting for the receiver Gaussian antenna pattern.

After accounting for the scattering event, the process restarts, this time with uniform random variables  $r_{ze}$  and  $r_{az}$  providing the zenith and azimuth scattering directions, and a new starting (scattered) Stokes vector  $\vec{I}_s$  is calculated from the product of the phase matrix  $\mathbf{Z}$  and the incident Stokes vector  $\vec{I}_i$ :

$$\vec{I}_s = \mathbf{Z}(\theta_i, \theta_s, \Delta\phi)\vec{I}_i \quad (28)$$

where  $\theta$  is the zenith angle and  $\Delta\phi$  is the difference of the scattered and incident azimuth angles. Subscripts  $i$  and  $s$  correspond to incident and scattered, respectively.

At subsequent scattering events, bistatic scattering for the incident and scattered angles contributes to the accumulated backscattering at the range bin corresponding to the total distance traveled before the scattering event. Path tracing ends, at an absorption event, when  $I$  falls below a predetermined threshold, or when the maximum specified scattering order is reached. A scattering order of 1 is equivalent to single scattering. For multiple scattering simulations, the suggested scattering order is 20 based on use across a range of cloud types.

Fig. 4 shows an example simulation, a hypothetical space-based nadir-pointing W-band radar, comparing single scattering (top panel) and multiple scattering (middle panel) simulations, with differences shown at the bottom. The top simulation uses the ARTS single scattering solver convolved with a Gaussian antenna pattern such that the field of view at the surface is 1 km. As expected, the largest multiple scattering enhancement corresponds to the convective cells and the surrounding regions. Multiple scattering results in excess reflectivity where the W-band signal is otherwise being extinguished, but this large enhancement is decorrelated from the vertical structure of the cloud along the radar line of sight. There are two features to note. The multiple scattering simulations are noisy at cloud edges and miss some thin clouds captured in the single scattering simulation. This is due to the large number of ray traces, on the order of 5e5, needed to resolve the simulations. While runtime is linear with the number of ray traces, the ray tracing routine is not trivial in terms of runtime. Thus, this simulator should be used only when multiple scattering is suspected.

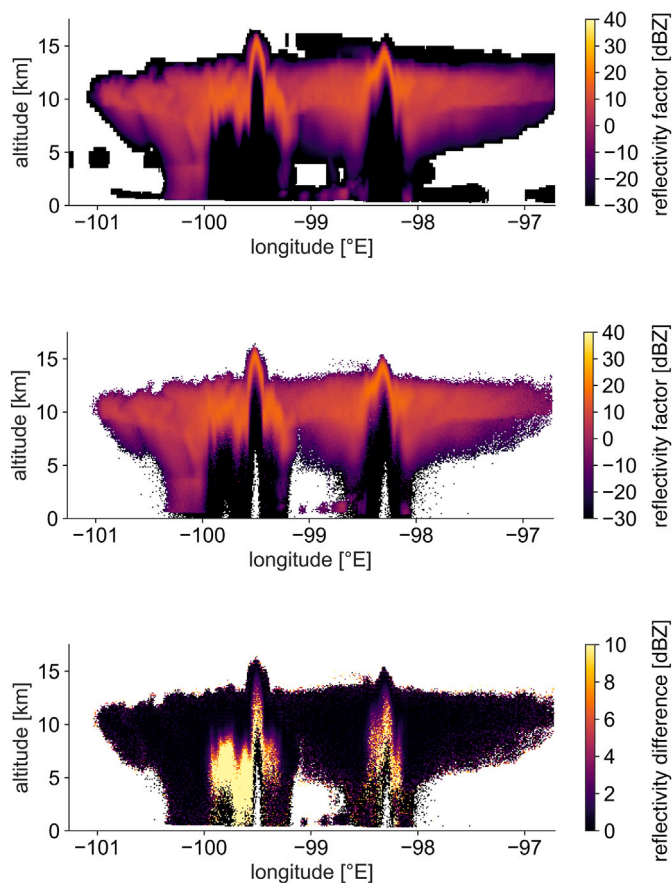


Fig. 4. Top panel: W-band single scattering simulation of convective cells and associated anvil. Middle panel: Multiple scattering simulation of same cloud field as top. Bottom panel: Difference of middle and top showing the enhancement due to multiple scattering.

## 5. Radiative energy flux and heating rate calculations

### 5.1. Fluxes

ARTS is suitable for accurate reference calculations of atmospheric energetics: radiative energy fluxes and associated heating rates. As an example, Roemer et al. [136] used it to investigate the longwave radiative feedback from a spectrally resolved perspective. To this end, spectral irradiance ( $\mathcal{L}_\nu$ ) at the top of the atmosphere was calculated for a set of idealized atmospheres, using the existing interface between ARTS and the single-column radiative-convective equilibrium model konrad [90,137]. Fig. 5 shows some of those  $\mathcal{L}_\nu$  spectra between  $10\text{ cm}^{-1}$  and  $2,500\text{ cm}^{-1}$  for surface temperatures of 268 K, 288 K, and 308 K, representing the spatial variations of Earth's surface temperature. Those simulations were then used to better understand the spectral longwave feedback derived from satellite observations.

Another very recent usage example of this capability is the study by He [138] that used ARTS for reference calculations of instantaneous  $4\times\text{CO}_2$  forcing at different surface temperatures.

Spectral irradiance is calculated by integrating the normal component of spectral radiance over one hemisphere [139, Equation 2.53], where spectral radiance is the first element of the Stokes vector introduced in Eq. (1). Integrating spectral irradiance over frequency then gives the total irradiance, that is, the total radiative energy flux in units of  $\text{W}/\text{m}^2$ . We define fluxes as a directed quantity in the context of 1D atmospheres, positive fluxes are directed upwards, negative fluxes are directed downwards, and the net flux is defined as the sum of the upward and downward flux.

ARTS has several ways to calculate radiation fluxes. For clear-sky fluxes there is an internal method, which uses the internal clear-sky radiative transfer solver to calculate spectral radiances. It assumes a plane parallel atmosphere, for consistency with the all-sky solvers described below.

For all-sky fluxes, one can in principle use any of the discrete ordinate solvers available in ARTS, that is DISORT, RT4 and DOIT to calculate spectral radiances and then integrate them as mentioned above using internal integration methods. Due to the higher complexity when handling scattering, all-sky flux simulations are in general several times slower than clear-sky flux simulations. To mitigate this, we recommend to use DISORT as it is much faster than RT4 and DOIT and advanced features of the other solvers like polarization are of less interest for flux calculations. Furthermore, ARTS supports a dedicated DISORT mode for simulating fluxes, in which the integration over the hemisphere is done internally and very efficiently.

The flux simulation can be done with an arbitrary number of zenith angles over which the angular integration is done, and an arbitrary number of frequencies over which the spectral integration is done. As a rule of thumb, to get an accuracy in the order of  $1\text{ W m}^{-2}$  for the fluxes, the number of zenith angles should be at least 6 and the number of frequencies should be in the order of several thousand. For reference calculations the number of frequencies should be even in the order of several ten thousand.

The left-hand columns of Figs. 6 and 7 illustrate ARTS' capability of simulating long wave and short wave net fluxes for different atmospheric conditions. Fig. 6 displays the results for a tropical atmosphere over the eastern Pacific with a thin liquid water cloud on top of the boundary layer and Fig. 7 for a summer atmosphere over the North Atlantic with various cloud layers and types. Reference flux calculations for all-sky and clear-sky were done using ARTS-DISORT with 30,000 frequencies and 10 streams.

An interesting option for efficient flux calculations is that ARTS ships with a set of representative frequencies and associated quadrature weights derived by Paulina Czarnecki [140]. Stated very briefly, the idea is that a weighted mean over the spectral flux at these few frequencies gives an accurate estimate of the total flux. They are identified from high spectral resolution reference calculations for a diverse set of atmospheres by a combination of simulated annealing and linear regression, a method that was originally developed for efficiently simulating satellite observations [10]. In this case there are 64 representative frequencies each for longwave and shortwave. The calculations with this method are  $30,000/64 \approx 470$  times faster than the reference calculations, results are marked with dots in Figs. 6 and 7, illustrating the close agreement.

### 5.2. Heating rates

Based on the fluxes, ARTS also calculates radiative heating rates. Assuming hydrostatic equilibrium, the heating rate  $H$  is defined as

$$H = \frac{g}{c_p} \frac{dF_{net}}{dp}, \quad (29)$$

where  $g$  is the gravitational acceleration,  $c_p$  is the mass specific heat capacity at constant pressure and  $F_{net}$  is the net flux. The derivative is internally approximated with central differences and for the edges with a polynomial interpolation, which both are second order accurate. With this approximation, the heating rates are calculated on the same grid as the atmospheric state. The gravitational acceleration  $g$  depends on altitude and latitude and is calculated internally (formally the function takes also longitude as input, but this is currently not used). The specific heat capacity  $c_p$  theoretically depends on temperature (and for a non-ideal gas it could even depend on pressure) and has to be provided by the user. For practical purposes, the temperature and pressure dependence results from the temperature and pressure dependence of the atmospheric composition. But since  $c_p$  varies only weakly for

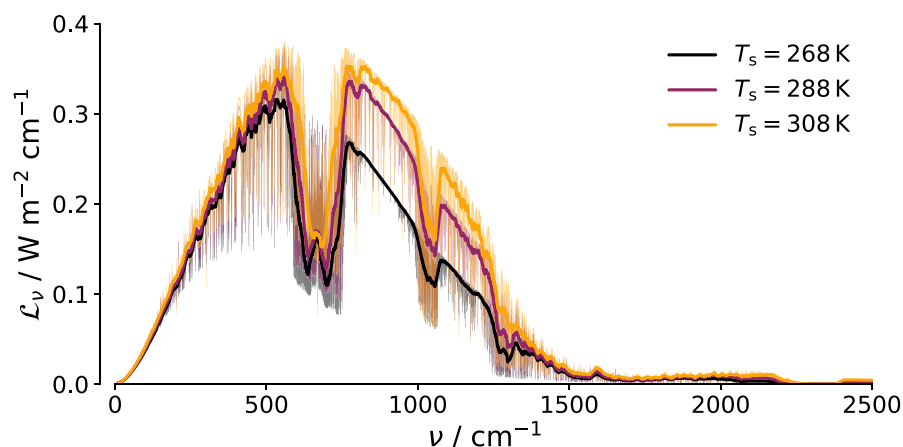


Fig. 5. Simulated spectrally resolved outgoing longwave radiation  $\mathcal{L}_\nu$  as a function of wavenumber  $\nu$  for idealized atmospheres with different surface temperatures  $T_s$ . Shown are the spectra at a spectral resolution of  $0.1 \text{ cm}^{-1}$  (thin lines, perhaps invisible in printed version) and the  $20 \text{ cm}^{-1}$  moving averages (thick lines).

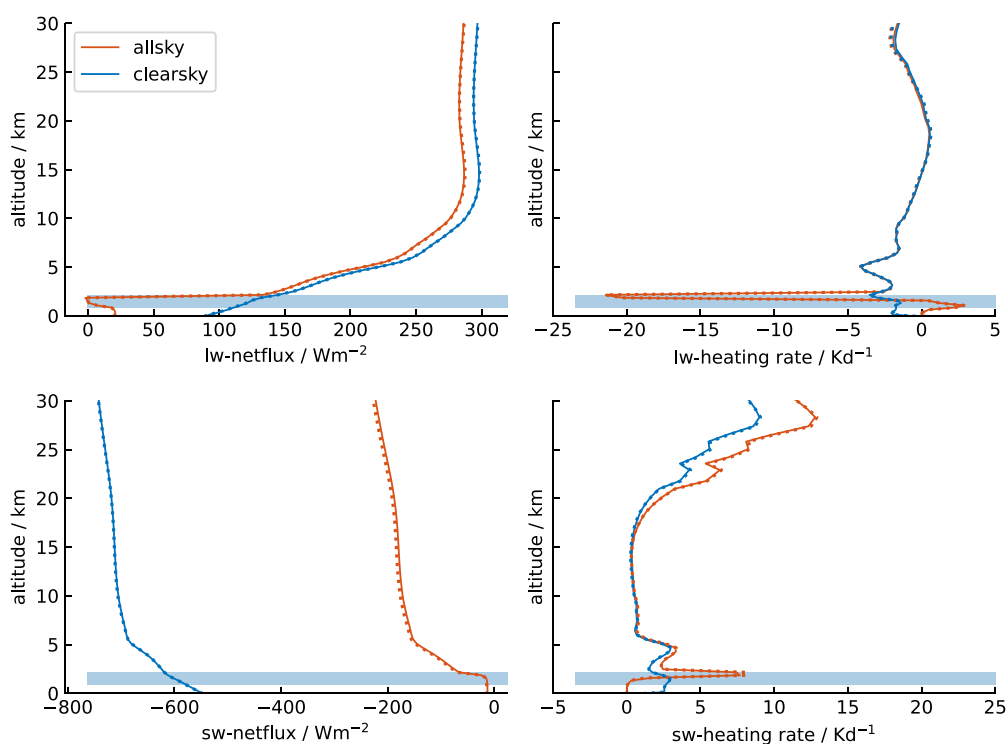


Fig. 6. Simulation results for a modeled tropical atmosphere over the eastern Pacific with a thin but dense liquid water cloud on top of the boundary layer (peak liquid water content  $0.4 \text{ g/m}^3$  at  $1.3 \text{ km}$  altitude, liquid water path  $500 \text{ g/m}^2$ ). Solid lines show the reference setup and dots show the fast setup. The blue shaded area indicates the position of the liquid water cloud. Top left: All sky and clear sky long wave net flux. Bottom left: All sky and clear sky short wave net flux. A positive net flux denotes a net upward flux and a negative net flux a net downward flux. Top right: All sky and clear sky long wave heating rates. Bottom right: All sky and clear sky short wave heating rates.

typical atmospheric conditions on Earth, it can be approximately set to a constant. In the following example,  $c_p$  is set constant to the mass specific heat capacity of dry air  $c_{p,air} = 1005.7 \text{ J kg}^{-1} \text{ K}^{-1}$  and  $g$  is varying with altitude.

The right columns of Figs. 6 and 7 show the all-sky and clear-sky long wave (top) and short wave (bottom) heating rates for the selected example cases. In Fig. 6 the liquid water cloud causes strong cooling in the long wave at the cloud top and weaker but also significant heating at the cloud bottom; in the short wave it causes some heating at the cloud top and suppresses the clear sky heating below. Dots again mark the fast approximation using the representative frequencies and weights. The very good agreement shows that the fast scheme is a very attractive option when spectral information is not needed. In Fig. 7 the clouds cause strong cooling in the long wave at the cloud tops and

weaker but also significant heating at the cloud bottoms except for the lowest cloud, where no heating occurs. In the short wave the clouds cause significant heating at the cloud tops in the middle and upper troposphere and suppress the clear sky heating below. At the lowest cloud the magnitude of sw-netflux is too small to create any significant amount of heating.

Note that the reason why the fast scheme works so well for heating rates is that heating rates were included as a training target, in addition to fluxes, in the derivation of the frequencies and weights [140]. This is necessary, because small fluctuations in the flux can have a large impact on its altitude gradient, the heating rate. This is particularly true at higher altitudes where the heat capacity is small due to low pressure.

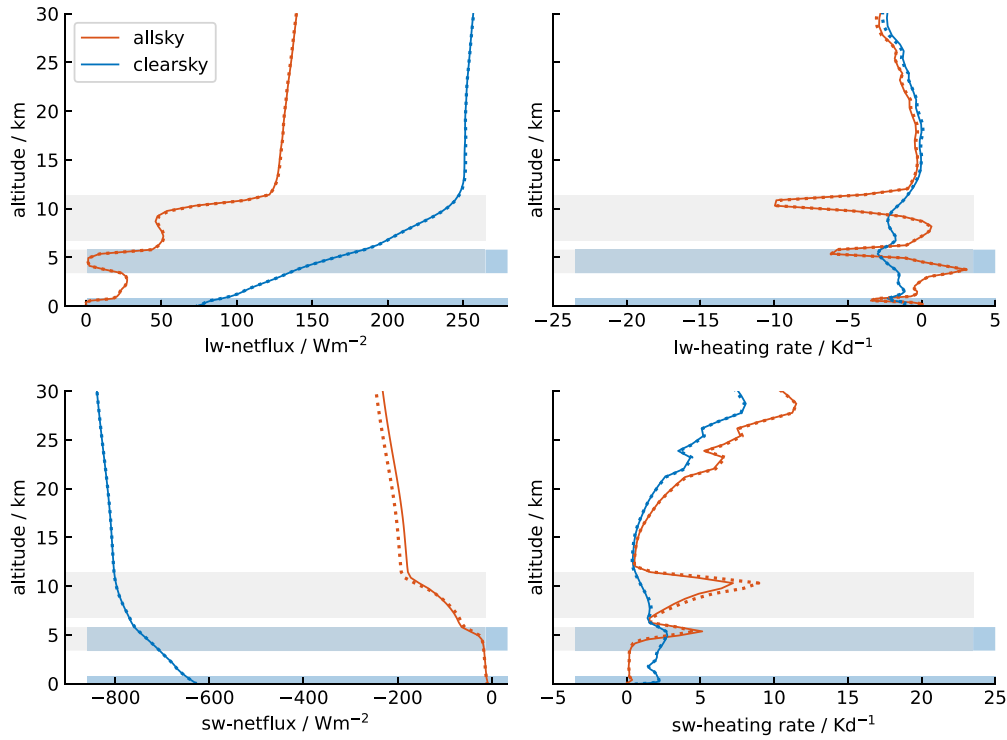


Fig. 7. Simulation results for a modeled summer atmosphere over the North Atlantic. It contains a thin low level liquid water cloud, a mid level mixed phase cloud, and a high level ice cloud (total liquid water path  $1450 \text{ g/m}^2$ , frozen water path  $93 \text{ g/m}^2$ ). Solid lines show the reference setup and dots show the fast setup. The blue shaded areas indicate the position of the liquid water clouds and the gray shaded areas the position of the frozen clouds. Top left: All sky and clear sky long wave net flux. Bottom left: All sky and clear sky short wave net flux. A positive net flux denotes a net upward flux and a negative net flux a net downward flux. Top right: All sky and clear sky long wave heating rates. Bottom right: All sky and clear sky short wave heating rates.

Note also, though, that the training for the representative frequencies and weights was completely based on clear-sky simulations. It is therefore not completely self-understood that they would work equally well for all-sky simulations, as the figure seems to indicate, although we had hypothesized that this would be the case. The argument in favor of this is that clouds tend to make the radiation field more homogeneous across different frequencies, which makes the exact positions of the quadrature frequencies less critical. We have not yet done a proper quantitative evaluation of the accuracy of the fast scheme for all-sky simulations, but these first results seem promising.

Finally, it is worth mentioning that the representative frequencies and weights so far were only trained for present-day variations of water vapor, ozone, temperature and different  $\text{CO}_2$  levels. There is work in progress on expanding that to variability in all greenhouse gases but for now the scheme will probably not work well for large perturbations in parameters not covered in the above list, for example for a significantly different methane concentration.

## 6. Optimal estimation retrievals

ARTS has supported retrievals since its first version by providing the Jacobian, but there has not been any built-in retrieval method. The standard alternative has been Qpack [4], providing a Matlab implementation of the optimal estimation method (OEM, [141]). OEM has now been integrated into ARTS, and, compared to [4], more efficient calculations and options can be offered.

### 6.1. Overview

The OEM is based on a Bayesian formulation of the inverse problem of finding an atmospheric state  $\vec{x}$  consistent with a vector  $\vec{y}$  of remote sensing observations using a forward model  $F : \vec{x} \rightarrow \vec{y}_f$  that allows simulating observations corresponding to a given atmospheric state

$\vec{x}$ . The OEM is based on the assumptions that (1) the error affecting the observations is bias-free Gaussian noise with covariance matrix  $\mathbf{S}_e$  and that (2) a priori knowledge of the atmospheric state  $\vec{x}$  can be described using a Gaussian distribution with a priori state  $\vec{x}_a$  and a priori covariance matrix  $\mathbf{S}_a$ . By application of Bayes' theorem, the posterior distribution, which fully describes the solution of the inverse problem, is found to be [141, Equation 2.24]:

$$p(\vec{x}|\vec{y}) = \exp\left(-\frac{1}{2}(\mathbf{F}(\vec{x}) - \vec{y})^T \mathbf{S}_e^{-1}(\mathbf{F}(\vec{x}) - \vec{y}) - \frac{1}{2}(\vec{x} - \vec{x}_a)^T \mathbf{S}_a^{-1}(\vec{x} - \vec{x}_a) + \text{const.}\right) \quad (30)$$

If the underlying assumptions of the OEM hold true, the posterior distribution is Gaussian, too, and is fully specified by its mean and covariance matrix. The mean of the posterior distribution, which, due to the Gaussian nature of the posterior distribution, coincides with the maximum a posteriori estimator of  $\vec{x}$ , is typically found by minimizing the negative log-likelihood of (30), which is given by

$$-\log(p(\vec{x}|\vec{y})) = \frac{1}{2}(\mathbf{F}(\vec{x}) - \vec{y})^T \mathbf{S}_e^{-1}(\mathbf{F}(\vec{x}) - \vec{y}) + \frac{1}{2}(\vec{x} - \vec{x}_a)^T \mathbf{S}_a^{-1}(\vec{x} - \vec{x}_a) \quad (31)$$

Finding the posterior mean state of the inverse problem thus boils down to minimizing Eq. (31). If the forward model  $F$  is linear, a global minimum of Eq. (31) can be found in a single step using the Gauss–Newton method. However, for most applications in atmospheric remote sensing the forward model  $F$  is non-linear. In this case, Eq. (31) has to be minimized iteratively. In addition to the Gauss–Newton (GN) method, the ARTS OEM method also provides an implementation of the Levenberg–Marquardt method (LM), which tends to be more stable for strongly non-linear forward models, such as those involving scattering.

Apart from the evaluation of the forward operator  $F$ , the computationally most complex operation in the application of the GN

and LM optimizers is the solving of a linear system of equations, having a size following the number of elements in  $\vec{x}$ . Since solving such a linear system of equations explicitly may become prohibitively expensive in terms of computation time and memory, all optimization methods in ARTS can be used with a conjugate gradient (CG) solver. The CG method solves the linear system iteratively and becomes computationally more efficient as the number of variables in  $\vec{x}$  grows large.

## 6.2. ARTS integration

The ARTS OEM method aims to retain most of ARTS' flexibility in terms of performing forward simulations. To provide a maximum of flexibility in terms of forward model calculations, the OEM module interfaces with the rest of ARTS by an agenda. This agenda typically performs the following steps:

1. Unpack the vector  $\vec{x}$  into the corresponding atmospheric fields and convert the elements to the forward model units,
2. perform the forward simulation,
3. apply required variable transformations to the Jacobian

Due to the flexibility of ARTS agendas this design allows most of ARTS' functionality to be used in a retrieval.

A principal benefit of the OEM integration into ARTS is that ARTS provides built-in functions that map elements of  $\vec{x}$  to atmospheric fields and back. Moreover, retrieval grids may deviate from the forward model grids. Although the retrieval grid is not allowed to be broader than the corresponding forward model grid, it can cover a smaller range. Retrieved values are mapped to the forward model grids by using linear interpolation inside the ranges of the retrieval grids, and using nearest neighbor outside. That is, values at end points of retrieval grids are assumed to be valid all the way to end points of the forward model grids. ARTS also provides functionality to retrieve transformed variables and apply clipping, which helps avoid unphysical states that may lead to errors in the forward model calculation.

## 6.3. Handling of a priori and observation error covariance matrices

The calculations required to perform an OEM minimization step involve only the inverses of the covariance matrices  $S_a$  and  $S_e$ . Since, depending on the retrieval problem at hand, the covariance matrices can grow relatively large, ARTS allows them to be provided either as  $S_a$  and  $S_e$  or directly as their inverses  $S_a^{-1}$  and  $S_e^{-1}$ , respectively. In conjunction with the CG solver, this can drastically reduce memory requirements of the OEM calculation step and thus allow for the retrieval of a larger number of variables and observations simultaneously.

ARTS covariance matrices are represented as block-diagonal matrices, where each block can be provided either as normal covariance matrix or its inverse. Moreover, covariance matrix blocks can be dense or sparse matrices. This design supports the basic use case in which the user simply provides the covariance matrices but also allows for optimization of the memory footprint of the inversion by providing pre-computed and potentially sparse covariance matrices. The full covariance matrix can be represented as a single block, to allow full generalization in the specification of correlations between variables.

## 7. Summary

This article gave an overview of the capabilities and limitations of ARTS version 2.6.

ARTS can compute atmospheric absorption by gases efficiently and accurately across the entire spectrum, from the radiowave to the UV/visible spectral range, including advanced features such as line mixing. Besides spectral line by spectral line absorption calculations, it also includes state of the art absorption continua, HITRAN

collision-induced absorption, and a simple polynomial model fitted to HITRAN absorption cross-sections, which can be used for example for halocarbon species for which spectroscopic data are typically not available [20].

In the longwave spectral range, ARTS is established and well tested for both clear-sky and all-sky radiative transfer simulations. In the clear-sky case (without scattering) it uses its own native radiative transfer solver, which includes analytical Jacobians. It is fully polarized and includes advanced features such as an accurate treatment of Zeeman splitting.

For all-sky radiative transfer simulation, ARTS offers broad support to cover microwave scattering due to hydrometeors. Inside this domain, the main consideration for the future is to improve the calculation efficiency. It is today costly to make simulations with a high number of scattering elements, and one way forward is to allow specifying bulk scattering properties directly. A full re-implementation of the handling of scattering data is ongoing to open up for this development, as well as obtaining a more uniform code base around the different scattering solvers.

Based on the radiative transfer simulations, ARTS can also perform energy flux and heating rate calculations for both clear-sky and all-sky conditions. Furthermore, it has built-in methods for optimal-estimation-type retrievals of atmospheric state properties from remote observations.

Very recently, ARTS was extended to include a solar source term, so that it can simulate also clear-sky and all-sky shortwave radiative transfer simulations and based on that shortwave energy fluxes and heating rates. This new functionality is the subject of a separate article that is currently in preparation. Calculations with the shortwave part have so far considered molecular (Rayleigh) scattering and scattering by hydrometeors. Aerosol scattering (and absorption) could in principle be handled as well, but so far there are no ready-made databases of aerosol optical properties in the ARTS format.

Last but not least, it should be mentioned that ARTS is also used as a teaching tool in the international Master program Atmospheric Science at University of Hamburg (<https://www.mi.uni-hamburg.de/studium/20-atmo-science.html>) for courses on radiation and climate and on remote sensing.

## Obtaining ARTS and contributing

The ARTS homepage, providing extensive documentation, is <https://radiativetransfer.org>. On GitHub, ARTS can be found at <https://github.com/atmtools/arts/releases>. For archiving purposes, there is also a package of the exact version described in this article on Zenodo [142].

The easiest way for Python users to obtain ARTS is through conda ('conda install -c rtools pyarts'). Pyarts is the python interface to ARTS, providing full ARTS functionality.

ARTS has been extensively tested and used on macOS, Linux, and other Unix systems. It has currently not been used or tested on Windows and there is also no conda package for Windows. This is planned to change for the next major version.

We welcome contributions. The for us most convenient way to contribute is through GitHub. Contributions can for example be bug fixes or extensions to the ARTS core, but also documentation, usage examples or helper tools.

Besides GitHub, a good way to communicate with other ARTS users and developers are the ARTS mailing lists (<https://www.radiativetransfer.org/contact>).

## CRedit authorship contribution statement

**Stefan A. Buehler:** Writing – review & editing, Writing – original draft, Investigation, Conceptualization. **Richard Larsson:** Writing – original draft, Software. **Oliver Lemke:** Writing – original draft, Software. **Simon Pfreundschuh:** Writing – original draft, Software. **Manfred Brath:** Writing – original draft, Software. **Ian Adams:** Writing – original draft, Software. **Stuart Fox:** Writing – original draft, Visualization. **Florian E. Roemer:** Writing – original draft, Visualization. **Paulina Czarnecki:** Writing – review & editing, Software. **Patrick Eriksson:** Writing – original draft, Software.

## Declaration of competing interest

The authors declare that they have no known competing financial interests or personal relationships that could have appeared to influence the work reported in this paper.

## Acknowledgments

We are grateful to Aistè Schunck for cleaning up the references, and we thank the ARTS community, in particular Vasileios Barlakas, Oleksandr Bobryshev, Jakob Dörr, Robin Ekelund, Gerrit Holl, gongx-unhij (Github handle), Lukas Kluff, Teresa Mendaza, Jana Mendrok, Jon Petersen, Marc Prange, Bengt Rydberg, Mayuri Tatiya and Takayoshi Yamada for contributing to the development of ARTS. We are also grateful to those that are active on the arts-users mailing list and help us respond to user questions.

For the Hamburg authors, this work is a contribution to the Centrum für Erdsystemforschung und Nachhaltigkeit (CEN). With its capabilities for calculating atmospheric energetics, ARTS also contributes to the Cluster of Excellence “CLICCS — Climate, Climatic Change, and Society”. The work at Chalmers by PE and SP was supported by the Swedish National Space Agency (grants 65/18 and 166/18).

## Appendix A. Supplementary data

Supplementary material related to this article can be found online at <https://doi.org/10.1016/j.jqsrt.2025.109443>.

## Data availability

ARTS is completely free. Section “Obtaining ARTS” describes how to obtain program and input data.

## References

- [1] Kuhn T, Bauer A, Godon M, Buehler SA, Kuenzi K. Water vapor continuum: Absorption measurements at 350 GHz and model calculations. *J Quant Spectrosc Radiat Transfer* 2002;74(5):545–62. [http://dx.doi.org/10.1016/S0022-4073\(01\)00271-0](http://dx.doi.org/10.1016/S0022-4073(01)00271-0).
- [2] Emde C, Buehler SA, Davis C, Eriksson P, Sreerekha TR, Teichmann C. A polarized discrete ordinate scattering model for simulations of limb and nadir longwave measurements in 1D/3D spherical atmospheres. *J Geophys Res* 2004;109(D24). <http://dx.doi.org/10.1029/2004JD005140>.
- [3] Sreerekha TR, Buehler SA, Emde C. A simple new radiative transfer model for simulating the effect of cirrus clouds in the Microwave Spectral Region. *J Quant Spectrosc Radiat Transfer* 2002;75:611–24.
- [4] Eriksson P, Jiménez C, Buehler SA. Opack, a general tool for instrument simulation and retrieval work. *J Quant Spectrosc Radiat Transfer* 2005;91(1):47–64. <http://dx.doi.org/10.1016/j.jqsrt.2004.05.050>.
- [5] Buehler SA, Eriksson P, Kuhn T, von Engeln A, Verdes C. ARTS, the atmospheric radiative transfer simulator. *J Quant Spectrosc Radiat Transfer* 2005;91(1):65–93. <http://dx.doi.org/10.1016/j.jqsrt.2004.05.051>.
- [6] Davis C, Emde C, Harwood R. A 3D polarized reversed Monte Carlo radiative transfer model for mm and sub-mm passive remote sensing in cloudy atmospheres. *IEEE T Geosci Remote* 2005;43(5):1096–101. <http://dx.doi.org/10.1109/TGRS.2004.837505>.

- [7] Melsheimer C, Verdes C, Buehler SA, Emde C, Eriksson P, Feist DG, Ichizawa S, John VO, Kasai Y, Kopp G, Koulev N, Kuhn T, Lemke O, Ochiai S, Schreier F, Sreerekha TR, Suzuki M, Takahashi C, Tsujimaru S, Urban J. Intercomparison of general purpose clear sky atmospheric radiative transfer models for the millimeter/submillimeter spectral range. *Radio Sci* 2005;40. <http://dx.doi.org/10.1029/2004RS003110>.
- [8] Buehler SA, von Engeln A, Brocard E, John VO, Kuhn T, Eriksson P. Recent developments in the line-by-line modeling of outgoing longwave radiation. *J Quant Spectrosc Radiat Transfer* 2006;98(3):446–57. <http://dx.doi.org/10.1016/j.jqsrt.2005.11.001>.
- [9] Eriksson P, Ekström M, Melsheimer C, Buehler SA. Efficient forward modelling by matrix representation of sensor responses. *Int J Remote Sens* 2007;27(9–10):1793–808. <http://dx.doi.org/10.1080/01431160500447254>.
- [10] Buehler SA, John VO, Kottayil A, Milz M, Eriksson P. Efficient radiative transfer simulations for a broadband infrared radiometer — Combining a weighted mean of representative frequencies approach with frequency selection by simulated annealing. *J Quant Spectrosc Radiat Transfer* 2010;111(4):602–15. <http://dx.doi.org/10.1016/j.jqsrt.2009.10.018>.
- [11] Buehler SA, Eriksson P, Lemke O. Updated lookup tables in the radiative transfer model ARTS. *J Quant Spectrosc Radiat Transfer* 2011;112(10):1559–67. <http://dx.doi.org/10.1016/j.jqsrt.2011.03.008>.
- [12] Eriksson P, Buehler SA, Davis CP, Emde C, Lemke O. ARTS, the atmospheric radiative transfer simulator, version 2. *J Quant Spectrosc Radiat Transfer* 2011;112(10):1551–8. <http://dx.doi.org/10.1016/j.jqsrt.2011.03.001>.
- [13] Larsson R, Buehler SA, Eriksson P, Mendrok J. A treatment of the Zeeman effect using Stokes formalism and its implementation in the Atmospheric Radiative Transfer Simulator (ARTS). *J Quant Spectrosc Radiat Transfer* 2014;133:445–53. <http://dx.doi.org/10.1016/j.jqsrt.2013.09.006>.
- [14] Larsson R. A note on modelling of the oxygen spectral cross-section in the Atmospheric Radiative Transfer Simulator — Zeeman effect combined with line mixing in earth’s atmosphere. *Int J Remote Sens* 2014;35(15):5845–53. <http://dx.doi.org/10.1080/01431161.2014.945002>.
- [15] Larsson R, Lankhaar B, Eriksson P. Updated Zeeman effect splitting coefficients for molecular oxygen in planetary applications. *J Quant Spectrosc Radiat Transfer* 2019;224:431–8. <http://dx.doi.org/10.1016/j.jqsrt.2018.12.004>.
- [16] Larsson R, Lankhaar B. Zeeman effect splitting coefficients for ClO, OH and NO in some earth atmosphere applications. *J Quant Spectrosc Radiat Transfer* 2020;250:107050. <http://dx.doi.org/10.1016/j.jqsrt.2020.107050>.
- [17] Eriksson P, Ekelund R, Mendrok J, Brath M, Lemke O, Buehler SA. A general database of hydrometeor single scattering properties at microwave and sub-millimetre wavelengths. *Earth Syst Sci Data* 2018;10(3):1301–26. <http://dx.doi.org/10.5194/essd-10-1301-2018>.
- [18] Brath M, Ekelund R, Eriksson P, Lemke O, Buehler SA. Microwave and submillimeter wave scattering of oriented ice particles. *Atmos Meas Tech* 2020;13:2309–33. <http://dx.doi.org/10.5194/amt-13-2309-2020>.
- [19] Kochanov RV, Gordon IE, Rothman LS, Shine KP, Sharpe SW, Johnson TJ, Wallington TJ, Harrison JJ, Bernath PF, Birk M, Wagner G, Le Bris K, Bravo I, Hill C. Infrared absorption cross-sections in HITRAN2016 and beyond: Expansion for climate, environment, and atmospheric applications. *J Quant Spectrosc Radiat Transfer* 2019;230:172–221. <http://dx.doi.org/10.1016/j.jqsrt.2019.04.001>.
- [20] Buehler SA, Brath M, Lemke O, Hodnebrog Ø, Pincus R, Eriksson P, Gordon I, Larsson R. A new halocarbon absorption model based on HITRAN cross-section data and new estimates of halocarbon instantaneous clear-sky radiative forcing. *J Adv Model Earth Syst* 2022;14(11). <http://dx.doi.org/10.1029/2022MS003239>.
- [21] Buehler SA, Mendrok J, Eriksson P, Perrin A, Larsson R, Lemke O. ARTS, the atmospheric radiative transfer simulator — version 2.2, the planetary toolbox edition. *Geosci Model Dev* 2018;11(4):1537–56. <http://dx.doi.org/10.5194/gmd-11-1537-2018>.
- [22] Mech M, Maahn M, Kneifel S, Ori D, Orlandi E, Kollias P, Schemann V, Crewell S. PAMTRA 1.0: the passive and active microwave radiative TRANSfer tool for simulating radiometer and radar measurements of the cloudy atmosphere. *Geosci Model Dev* 2020;13(9):4229–51. <http://dx.doi.org/10.5194/gmd-13-4229-2020>.
- [23] Schreier F, Garcia SG, Hochstaffl P, Staedt S. Py4CAtSPYthon for computational atmospheric spectroscopy. *Atmosphere* 2019;10(5). <http://dx.doi.org/10.3390/atmos10050262>.
- [24] Gordon I, Rothman L, Hargreaves R, Hashemi R, Karlovets E, Skinner F, Conway E, Hill C, Kochanov R, Tan Y, Wcislo P, Finenko A, Nelson K, Bernath P, Birk M, Boudon V, Campargue A, Chance K, Coustenis A, Drouin B, Flaud J-M, Gamache R, Hodges J, Jacquemart D, Mlawer E, Nikitin A, Perevalov V, Rotger M, Tennyson J, Toon G, Tran H, Tyuterev V, Adkins E, Baker A, Barbe A, Canè E, Császár A, Dudaryonok A, Egorov O, Fleisher A, Fleurbaey H, Foltynowicz A, Furtenbacher T, Harrison J, Hartmann J-M, Horneman V-M, Huang X, Karman T, Karns J, Kassi S, Kleiner I, Kofman V, Kwabia-Tchana F, Lavrentieva N, Lee T, Long D, Lukashevskaya A, Lyulin O, Makhnev V, Matt W, Massie S, Melosso M, Mikhalenko S, Mondelain D, Müller H, Naumenko O, Perrin A, Polyansky O, Raddaoui E, Raston P, Reid Z, Rey M, Richard C, Tóbiás R, Sadiek I, Schwenke D, Starikova E, Sung K,

- Tamassia F, Tashkun S, Vander Auwera J, Vasilenko I, Viginas A, Villanueva G, Vispoel B, Wagner G, Yachmenev A, Yurchenko S. The HITRAN2020 molecular spectroscopic database. *J Quant Spectrosc Radiat Transfer* 2022;277:107949. <http://dx.doi.org/10.1016/j.jqsrt.2021.107949>.
- [25] Arendas P, Furtenbacher T, Csaszar AG. Selecting lines for spectroscopic (re)measurements to improve the accuracy of absolute energies of rovibronic quantum states. *J Cheminform* 2021;13(1). <http://dx.doi.org/10.1186/s13321-021-00534-y>.
- [26] Wang W, Murk A, Sauvageat E, Fan W, Daetwyler C, Hervo M, Haeferle A, Hocke K. An indoor microwave radiometer for measurement of tropospheric water. *IEEE T Geosci Remote* 2023;61. <http://dx.doi.org/10.1109/TGRS.2023.3261067>.
- [27] Schranz F, Tschanz B, Ruefenacht R, Hocke K, Palm M, Kaempfer N. Investigation of Arctic middle-atmospheric dynamics using 3 years of H<sub>2</sub>O and O<sub>3</sub> measurements from microwave radiometers at Ny-Alesund. *Atmos Chem Phys* 2019;19(15):9927–47. <http://dx.doi.org/10.5194/acp-19-9927-2019>.
- [28] Lainer M, Hocke K, Kampfer N. Long-term observation of midlatitude quasi 2-day waves by a water vapor radiometer. *Atmos Chem Phys* 2018;18(16):12061–74. <http://dx.doi.org/10.5194/acp-18-12061-2018>.
- [29] Mevi G, Muscari G, Bertagnolio PP, Fiorucci I, Pace G. VESPA-22: a ground-based microwave spectrometer for long-term measurements of polar stratospheric water vapor. *Atmos Meas Tech* 2018;11(2):1099–117. <http://dx.doi.org/10.5194/amt-11-1099-2018>.
- [30] Pan L, Lu D. Terahertz band simulations using two different radiative transfer models. *Sci China- Earth Sci* 2018;61(10):1482–90. <http://dx.doi.org/10.1007/s11430-017-9242-3>.
- [31] Sauvageat E, Albers R, Kotiranta M, Hocke K, Gomez RM, Nedoluha G, Murk A. Comparison of Three High Resolution Real-Time Spectrometers for Microwave Ozone Profiling Instruments. *IEEE J Sel Top Appl Rem Sens* 2021;14:10045–56. <http://dx.doi.org/10.1109/JSTARS.2021.3114446>.
- [32] Schranz F, Fernandez S, Kaempfer N, Palm M. Diurnal variation in middle-atmospheric ozone observed by ground-based microwave radiometry at Ny-Alesund over 1 year. *Atmos Chem Phys* 2018;18(6):4113–30. <http://dx.doi.org/10.5194/acp-18-4113-2018>.
- [33] Bernet L, von Clarmann T, Godin-Beekmann S, Ancellet G, Barras EM, Stubi R, Steinbrecht W, Kampfer N, Hocke K. Ground-based ozone profiles over central Europe: incorporating anomalous observations into the analysis of stratospheric ozone trends. *Atmos Chem Phys* 2019;19(7):4289–309. <http://dx.doi.org/10.5194/acp-19-4289-2019>.
- [34] Newnham DA, Clilverd MA, Clark WDJ, Kosch M, Verronen PT, Rogers AEE. Ground-based Ku-band microwave observations of ozone in the polar middle atmosphere. *Atmos Meas Tech* 2022;15(8):2361–76. <http://dx.doi.org/10.5194/amt-15-2361-2022>.
- [35] Moreira L, Hocke K, Kaempfer N. Short-term stratospheric ozone fluctuations observed by GROMOS microwave radiometer at Bern. *Earth Planets Space* 2018;70. <http://dx.doi.org/10.1186/s40623-017-0774-4>.
- [36] Ryan NJ, Palm M, Hoffmann CG, Goliash J, Notholt J. Ground-based millimetre-wave measurements of middle-atmospheric carbon monoxide above Ny-Alesund (78.9 degrees N, 11.9 degrees E). *Atmos Meas Tech* 2019;12(7):4077–89. <http://dx.doi.org/10.5194/amt-12-4077-2019>.
- [37] Shi Y, Shulga V, Ivaniha O, Wang Y, Evtushevsky O, Milinevsky G, Klekociuk A, Patoka A, Han W, Shulga D. Comparison of Major Sudden Stratospheric Warming Impacts on the Mid-Latitude Mesosphere Based on Local Microwave Radiometer CO Observations in 2018 and 2019. *Rem Sens* 2020;12(23). <http://dx.doi.org/10.3390/rs12233950>.
- [38] Wang Y, Shulga V, Milinevsky G, Patoka A, Evtushevsky O, Klekociuk A, Han W, Grytsai A, Shulga D, Myshenko V, Antyufeyev O. Winter 2018 major sudden stratospheric warming impact on midlatitude mesosphere from microwave radiometer measurements. *Atmos Chem Phys* 2019;19(15):10303–17. <http://dx.doi.org/10.5194/acp-19-10303-2019>.
- [39] Krochin W, Navas-Guzman F, Kuhl D, Murk A, Stober G. Continuous temperature soundings at the stratosphere and lower mesosphere with a ground-based radiometer considering the Zeeman effect. *Atmos Meas Tech* 2022;15(7):2231–49. <http://dx.doi.org/10.5194/amt-15-2231-2022>.
- [40] Hagen J, Hocke K, Stober G, Pfreundschuh S, Murk A, Kaempfer N. First measurements of tides in the stratosphere and lower mesosphere by ground-based Doppler microwave wind radiometry. *Atmos Chem Phys* 2020;20(4):2367–86. <http://dx.doi.org/10.5194/acp-20-2367-2020>.
- [41] Hagen J, Murk A, Rufenacht R, Khaykin S, Hauchecorne A, Kampfer N. WIRA-C: a compact 142-GHz-radiometer for continuous middle-atmospheric wind measurements. *Atmos Meas Tech* 2018;11(9):5007–24. <http://dx.doi.org/10.5194/amt-11-5007-2018>.
- [42] Lang T, Buehler SA, Burgdorf M, Hans I, John VO. A new climate data record of upper-tropospheric humidity from microwave observations. *Sci Data* 2020;7(218). <http://dx.doi.org/10.1038/s41597-020-0560-1>.
- [43] Prange M, Brath M, Buehler SA. Are elevated moist layers a blind spot for hyperspectral infrared sounders? – a model study. *Atmos Meas Tech* 2021;14(11):7025–44. <http://dx.doi.org/10.5194/amt-14-7025-2021>.
- [44] He J, Chen H. Atmospheric retrievals and assessment for microwave observations from Chinese FY-3C satellite during hurricane matthew. *Rem Sens* 2019;11(8). <http://dx.doi.org/10.3390/rs11080896>.
- [45] Schreier F, Milz M, Buehler SA, von Clarmann T. Intercomparison of three microwave/infrared high resolution line-by-line radiative transfer codes. *J Quant Spectrosc Radiat Transfer* 2018;211:64–77. <http://dx.doi.org/10.1016/j.jqsrt.2018.02.032>.
- [46] Bobryshev O, Buehler SA, John VO, Brath M, Brogniez H. Is there really a closure gap between 183.31 GHz satellite passive microwave and in-situ radiosonde water vapor measurements? *IEEE T Geosci Remote* 2018;56(5):2904–10. <http://dx.doi.org/10.1109/TGRS.2017.2786548>.
- [47] Moradi I, Goldberg M, Brath M, Ferraro R, Buehler SA, Saunders R, Sun N. Performance of radiative transfer models in the microwave region. *J Geophys Res Atm* 2020;125(6):e2019JD031831. <http://dx.doi.org/10.1029/2019JD031831>.
- [48] Scarlat RC, Melsheimer C, Heygster G. Retrieval of total water vapour in the Arctic using microwave humidity sounders. *Atmos Meas Tech* 2018;11(4):2067–84. <http://dx.doi.org/10.5194/amt-11-2067-2018>.
- [49] He W, Wang Z, Wang W, Zhang Z. Sensitivity analysis of microwave spectrometer for atmospheric temperature and humidity sounding on the new generation fengyun satellite. *IEEE J Sel Top Appl Rem Sens* 2023;16:853–65. <http://dx.doi.org/10.1109/JSTARS.2022.3230845>.
- [50] Sheese PE, Walker KA, Boone CD, Bourassa AE, Degenstein DA, Froidevaux L, McElroy CT, Murtagh D, Iii JMR, Zou J. Assessment of the quality of ACE-FTS stratospheric ozone data. *Atmos Meas Tech* 2022;15(5):1233–49. <http://dx.doi.org/10.5194/amt-15-1233-2022>.
- [51] Xu H, Lu H, Wang Z, He W, Wang W. Effect analysis of the digital spectrometer FFT algorithm on THz atmospheric limb sounder (TALIS) system sensitivity. *Rem Sens* 2021;13(15). <http://dx.doi.org/10.3390/rs13152921>.
- [52] Yamada T, Sato TO, Adachi T, Winkler H, Kuribayashi K, Larsson R, Yoshida N, Takahashi Y, Sato M, Chen AB, Hsu RR, Nakano Y, Fujinawa T, Nara S, Uchiyama Y, Kasai Y. HO<sub>2</sub> generation above sprite-producing thunderstorms derived from low-noise SMILES observation spectra. *Geophys Res Lett* 2020;47(3). <http://dx.doi.org/10.1029/2019GL085529>.
- [53] Grieco F, Perot K, Murtagh D, Eriksson P, Rydberg B, Kiefer M, Garcia-Comas M, Lambert A, Walker KA. Improvement of odin/SMR water vapour and temperature measurements and validation of the obtained data sets. *Atmos Meas Tech* 2021;14(8):5823–57. <http://dx.doi.org/10.5194/amt-14-5823-2021>.
- [54] Wang W, Wang Z, Duan Y. Performance evaluation of THz atmospheric limb sounder (TALIS) of China. *Atmos Meas Tech* 2020;13(1):13–38. <http://dx.doi.org/10.5194/amt-13-13-2020>.
- [55] Duan Y, Wang Z, Xu H, Wang W. Simulation of the spectrum response for the THz atmosphere limb sounder (TALIS). *Sensors* 2020;20(2). <http://dx.doi.org/10.3390/s20020498>.
- [56] Song R, Kaufmann M, Ern M, Ungermann J, Liu G, Riese M. Three-dimensional tomographic reconstruction of atmospheric gravity waves in the mesosphere and lower thermosphere (MLT). *Atmos Meas Tech* 2018;11(5):3161–75. <http://dx.doi.org/10.5194/amt-11-3161-2018>.
- [57] Li-cheng L, Hai-yang G, Ling-bing B, Qi-lin Z, Zhen W. Inversion of rotational temperature in airglow layer based on O-2 (0-1) atmospheric band spectrum. *Spectrosc Spectr Anal* 2020;40(10):3002–9. [http://dx.doi.org/10.3964/j.issn.1000-0593\(2020\)10-3002-08](http://dx.doi.org/10.3964/j.issn.1000-0593(2020)10-3002-08).
- [58] Gao H, Li L, Bu L, Zhang Q, Wang Z, Tang Y. Measurement of mesopause temperature using the mesospheric airglow spectrum photometer (MASP). *Opt Commun* 2020;464. <http://dx.doi.org/10.1016/j.optcom.2020.125546>.
- [59] Pfreundschuh S, Eriksson P, Duncan D, Rydberg B, Hakansson N, Thoss A. A neural network approach to estimating a posteriori distributions of Bayesian retrieval problems. *Atmos Meas Tech* 2018;11(8):4627–43. <http://dx.doi.org/10.5194/amt-11-4627-2018>.
- [60] Adams IS, Munchak SJ, Kuo K-S, Pelissier C, Clune T, Kroodsma R, Loftus A, Li X. Active and passive radiative transfer simulations for GMP-related field campaigns. In: 2019 IEEE international geoscience and remote sensing symposium (IGARSS 2019). IEEE international symposium on geoscience and remote sensing IGARSS, Inst Elect & Elect Engineers; Inst Elect & Elect Engineers, Geoscience & Remote Sensing Soc; 2019, p. 4553–6.
- [61] Grützun V, Buehler SA, Kluff L, Brath M, Mendrok J, Eriksson P. All-sky information content analysis for novel passive microwave instruments in the range from 23.8 GHz up to 874.4 GHz. *Atmos Meas Tech* 2018;11(7):4217–37. <http://dx.doi.org/10.5194/amt-11-4217-2018>.
- [62] Liu Y, Mace GG. Assessing synergistic radar and radiometer capability in retrieving ice cloud microphysics based on hybrid Bayesian algorithms. *Atmos Meas Tech* 2022;15(4):927–44. <http://dx.doi.org/10.5194/amt-15-927-2022>.
- [63] Geer AJ, Bauer P, Lonitz K, Barlakas V, Eriksson P, Mendrok J, Doherty A, Hocking J, Chambon P. Bulk hydrometeor optical properties for microwave and sub-millimetre radiative transfer in RTTOV-SCATT v13.0. *Geosci Model Dev* 2021;14(12):7497–526. <http://dx.doi.org/10.5194/gmd-14-7497-2021>.
- [64] Li S, Liu L, Letu H, Hu S, Dong P, Ren H, Ye J. Evaluation of the impacts of ice cloud vertical inhomogeneity on spaceborne passive submillimeter-wave simulations. *Q J R Meteorol Soc* 2023;149(752):1073–89. <http://dx.doi.org/10.1002/qj.4457>.
- [65] Peers F, Francis P, Abel SJ, Barrett PA, Bower KN, Cotterell IM, Crawford I, Davies NW, Fox C, Fox S, Langridge JM, Meyer KG, Platnick SE, Szpek K, Hayward JM. Observation of absorbing aerosols above clouds over the south-east Atlantic ocean from the geostationary satellite SEVIRI - Part 2: Comparison

- with MODIS and aircraft measurements from the CLARIFY-2017 field campaign. *Atmos Chem Phys* 2021;21(4):3235–54. <http://dx.doi.org/10.5194/acp-21-3235-2021>.
- [66] Brath M, Fox S, Eriksson P, Harlow RC, Burgdorf M, Buehler SA. Retrieval of an ice water path over the ocean from ISMAR and MARSS millimeter and submillimeter brightness temperatures. *Atmos Meas Tech* 2018;11:611–32. <http://dx.doi.org/10.5194/amt-11-611-2018>.
- [67] Leppert II KD, Cecil DJ. Sensitivity of simulated GMI brightness temperatures to variations in particle size distributions in a severe hailstorm. *J Appl Meteorol Clim* 2019;58(9):1905–30. <http://dx.doi.org/10.1175/JAMC-D-19-0031.1>.
- [68] Pfreundschuh S, Eriksson P, Buehler SA, Brath M, Duncan D, Larsson R, Ekelund R. Synergistic radar and radiometer retrievals of ice hydrometeors. *Atmos Meas Tech* 2020;13(8):4219–45. <http://dx.doi.org/10.5194/amt-13-4219-2020>.
- [69] Pfreundschuh S, Fox S, Eriksson P, Duncan D, Buehler SA, Brath M, Cotton R, Ewald F. Synergistic radar and sub-millimeter radiometer retrievals of ice hydrometeors in mid-latitude frontal cloud systems. *Atmos Meas Tech* 2022;15(3):677–99. <http://dx.doi.org/10.5194/amt-15-677-2022>.
- [70] Liu Y, Mace GG. Synthesizing the vertical structure of tropical cirrus by combining CloudSat radar reflectivity with in situ microphysical measurements using Bayesian Monte Carlo integration. *J Geophys Res Atm* 2020;125(18). <http://dx.doi.org/10.1029/2019JD031882>.
- [71] Gong J, Wu DL, Eriksson P. The first global 883 GHz cloud ice survey: IceCube Level 1 data calibration, processing and analysis. *Earth Syst Sci Data* 2021;13(11):5369–87. <http://dx.doi.org/10.5194/essd-13-5369-2021>.
- [72] Barlakas V, Eriksson P. Three dimensional radiative effects in passive millimeter/sub-millimeter all-sky observations. *Rem Sens* 2020;12(3). <http://dx.doi.org/10.3390/rs12030531>.
- [73] Aires F, Prigent C, Buehler SA, Eriksson P, Milz M, Crewell S. Towards more realistic hypotheses for the information content analysis of cloudy/precipitating situations - Application to a hyperspectral instrument in the microwave. *Q J R Meteorol Soc* 2019;145(718, A):1–14. <http://dx.doi.org/10.1002/qj.3315>.
- [74] Ekelund R, Eriksson P, Pfreundschuh S. Using passive and active observations at microwave and sub-millimeter wavelengths to constrain ice particle models. *Atmos Meas Tech* 2020;13(2):501–20. <http://dx.doi.org/10.5194/amt-13-501-2020>.
- [75] Barlakas V, Galligani VS, Geer AJ, Eriksson P. On the accuracy of RTTOV-SCATT for radiative transfer at all-sky microwave and submillimeter frequencies. *J Quant Spectrosc Radiat Transfer* 2022;283:108137. <http://dx.doi.org/10.1016/j.jqsrt.2022.108137>.
- [76] Fox S, Mendrok J, Eriksson P, Ekelund R, O'Shea SJ, Bower KN, Baran AJ, Harlow RC, Pickering JC. Airborne validation of radiative transfer modelling of ice clouds at millimeter and sub-millimeter wavelengths. *Atmos Meas Tech* 2019;12(3):1599–617. <http://dx.doi.org/10.5194/amt-12-1599-2019>.
- [77] Casella D, Panegrossi G, Sano P, Rydberg B, Mattioli V, Accadia C, Papa M, Marzano FS, Montopoli M. Can we use atmospheric targets for geolocating spaceborne millimeter-wave ice cloud imager (ICI) acquisitions? *IEEE T Geosci Remote* 2022;60. <http://dx.doi.org/10.1109/TGRS.2022.3145638>.
- [78] Liu Y, Buehler SA, Brath M, Liu H, Dong X. Ensemble optimization retrieval algorithm of hydrometeor profiles for the ice cloud imager submillimeter-wave radiometer. *J Geophys Res Atm* 2018;123(9):4594–612. <http://dx.doi.org/10.1002/2017JD027892>.
- [79] Eriksson P, Rydberg B, Mattioli V, Thoss A, Accadia C, Klein U, Buehler SA. Towards an operational Ice Cloud Imager (ICI) retrieval product. *Atmos Meas Tech* 2020;13:53–71. <http://dx.doi.org/10.5194/amt-13-53-2020>.
- [80] Galligani VS, Wang D, Corrales PB, Prigent C. A parameterization of the cloud scattering polarization signal derived from GPM observations for microwave fast radiative transfer models. *IEEE T Geosci Remote* 2021;59(11):8968–77. <http://dx.doi.org/10.1109/TGRS.2021.3049921>.
- [81] Coy JJ, Bell A, Yang P, Wu DL. Sensitivity analyses for the retrievals of ice cloud properties from radiometric and polarimetric measurements in sub-mm/mm and infrared bands. *J Geophys Res Atm* 2020;125(13). <http://dx.doi.org/10.1029/2019JD031422>.
- [82] Dong P, Liu L, Li S, Hu S, Bu L. Application of M5 model tree in passive remote sensing of thin ice cloud microphysical properties in terahertz region. *Rem Sens* 2021;13(13). <http://dx.doi.org/10.3390/rs13132569>.
- [83] Weng C, Liu L, Gao T, Hu S, Li S, Dou F, Shang J. Multi-channel regression inversion method for passive remote sensing of ice water path in the terahertz band. *Atmosphere* 2019;10(8). <http://dx.doi.org/10.3390/atmos10080437>.
- [84] Liu L, Weng C, Li S, Husi L, Hu S, Dong P. Passive remote sensing of ice cloud properties at terahertz wavelengths based on genetic algorithm. *Rem Sens* 2021;13(4). <http://dx.doi.org/10.3390/rs13040735>.
- [85] Shu-Lei L, Lei L, Tai-Chang G, Li-Huai S, Shi Q, Shuai H. Radiation characteristics of the selected channels for cirrus remote sensing in terahertz waveband and the influence factors for the retrieval method. *JIMW* 2018;37(1):60–71. <http://dx.doi.org/10.11972/j.issn.1001-9014.2018.01.012>.
- [86] Li H-Y, Wu Z-S, Wu J-J, Lin L-K, Lu C-S, Zhao Z-W, Qu T. THz wave background radiation at upper troposphere. *Multimed Tools Appl* 2020;79(13–14):8767–80. <http://dx.doi.org/10.1007/s11042-018-6803-x>.
- [87] Cutraro F, Galligani VS, Garcia Skabar Y. Evaluation of synthetic satellite images computed from radiative transfer models over a region of South America using WRF and GOES-13/16 observations. *Q J R Meteorol Soc* 2021;147(738):2988–3003. <http://dx.doi.org/10.1002/qj.4111>.
- [88] Pincus R, Buehler SA, Brath M, Crevoisier C, Jamil O, Evans KF, Manners J, Menzel RL, Mlawer EJ, Paynter D, Pernak RL, Tellier Y. Benchmark calculations of radiative forcing by greenhouse gases. *J Geophys Res Atm* 2020;123(23):e2020JD033483. <http://dx.doi.org/10.1029/2020JD033483>.
- [89] Bourdin S, Kluft L, Stevens B. Dependence of climate sensitivity on the given distribution of relative humidity. *Geophys Res Lett* 2021;48(8). <http://dx.doi.org/10.1029/2021GL092462>.
- [90] Kluft L, Dacie S, Buehler SA, Schmidt H, Stevens B. Re-examining the first climate models: Climate sensitivity of a modern radiative-convective equilibrium model. *J Clim* 2019;32(23):8111–25. <http://dx.doi.org/10.1175/JCLI-D-18-0774.1>.
- [91] Kluft L, Dacie S, Brath M, Buehler SA, Stevens B. Temperature-dependence of the clear-sky feedback in radiative-convective equilibrium. *Geophys Res Lett* 2021;48(22). <http://dx.doi.org/10.1029/2021GL094649>.
- [92] Gao M, Franz BA, Knobelspiesse K, Zhai P-W, Martins V, Burton S, Cairns B, Ferrare R, Gales J, Hasekamp O, Hu Y, Ibrahim A, McBride B, Puthukkudy A, Werdell PJ, Xu X. Efficient multi-angle polarimetric inversion of aerosols and ocean color powered by a deep neural network forward model. *Atmos Meas Tech* 2021;14(6):4083–110. <http://dx.doi.org/10.5194/amt-14-4083-2021>.
- [93] Emde C, Yu H, Kylling A, van Roozendaal M, Stebel K, Veihelmann B, Mayer B. Impact of 3D cloud structures on the atmospheric trace gas products from UV-Vis sounders - Part 1: Synthetic dataset for validation of trace gas retrieval algorithms. *Atmos Meas Tech* 2022;15(5):1587–608. <http://dx.doi.org/10.5194/amt-15-1587-2022>.
- [94] Yu H, Emde C, Kylling A, Veihelmann B, Mayer B, Stebel K, Van Roozendaal M. Impact of 3D cloud structures on the atmospheric trace gas products from UV-Vis sounders - Part 2: Impact on NO<sub>2</sub> retrieval and mitigation strategies. *Atmos Meas Tech* 2022;15(19):5743–68. <http://dx.doi.org/10.5194/amt-15-5743-2022>.
- [95] Mathew N, Sahoo S, Pillai RR, Raju CS. Millimeter-wave radiometric information content analysis for venus atmospheric constituents. *Radio Sci* 2020;55(2). <http://dx.doi.org/10.1029/2019RS006913>.
- [96] Larsson R, Kasai Y, Kuroda T, Sato S, Yamada T, Maezawa H, Hasegawa Y, Nishibori T, Nakasuka S, Hartogh P. Mars submillimeter sensor on microsatellite: sensor feasibility study. *Geosci Instr Methods Data Syst* 2018;7(4):331–41. <http://dx.doi.org/10.5194/gi-7-331-2018>.
- [97] Duncan DI, Eriksson P, Pfreundschuh S. An experimental 2D-var retrieval using AMSR2. *Atmos Meas Tech* 2019;12(12):6341–59. <http://dx.doi.org/10.5194/amt-12-6341-2019>.
- [98] Ciani D, Sabatini M, Nardelli BB, Dekker PL, Rommen B, Wethy DS, Yang C, Liberti GL. Sea surface temperature gradients estimation using top-of-atmosphere observations from the ESA earth explorer 10 harmony mission: Preliminary studies. *Rem Sens* 2023;15(4). <http://dx.doi.org/10.3390/rs15041163>.
- [99] Jakob W, Rhineland J, Moldovan D. pybind11 – Seamless operability between C++ and Python. 2017. <https://github.com/pybind/pybind11>.
- [100] Mlawer EJ, Cady-Pereira KE, Mascio J, Gordon IE. The inclusion of the MT\_CKD water vapor continuum model in the HITRAN molecular spectroscopic database. *J Quant Spectrosc Radiat Transfer* 2023;306:108645. <http://dx.doi.org/10.1016/j.jqsrt.2023.108645>.
- [101] Shine KP, Ptashnik IV, Rädcl G. The water vapour continuum: Brief history and recent developments. *Sur Geophy* 2012;33:535–55. <http://dx.doi.org/10.1007/s10712-011-9170-y>.
- [102] Schwarzschild K. Ueber das Gleichgewicht der Sonnenatmosphäre. *Nachrichten von der Ges der Wiss zu Göttingen, Mathematisch- Phys Kl* 1906;1906(1):41–53.
- [103] Baron P, Ochiai S, Dupuy E, Larsson R, Liu H, Manago N, Murtagh D, Oyama S, Sagawa H, Saito A, Sakazaki T, Shiotani M, Suzuki M. Potential for the measurement of mesosphere and lower thermosphere (MLT) wind, temperature, density and geomagnetic field with superconducting submillimeter-wave limb-emission sounder 2 (SMILES-2). *Atmos Meas Tech* 2020;13(1):219–37. <http://dx.doi.org/10.5194/amt-13-219-2020>.
- [104] Moler C, Van Loan C. Nineteen dubious ways to compute the exponential of a matrix, twenty-five years later. *SIAM Rev* 2003;45(1):3–49. <http://dx.doi.org/10.1137/S00361445024180>.
- [105] Stamnes K, Thomas GE, Stamnes JJ. Radiative transfer in the atmosphere and ocean (2nd edition). Cambridge University Press; 2017, p. 79. <http://dx.doi.org/10.1017/9781316148549>.
- [106] Buras R, Dowling T, Emde C. New secondary-scattering correction in DISORT with increased efficiency for forward scattering. *J Quant Spectrosc Radiat Transfer* 2011;112(12):2028–34.
- [107] Bates D. Rayleigh scattering by air. *Planet Space Sci* 1984;32(6):785–90. [http://dx.doi.org/10.1016/0032-0633\(84\)90102-8](http://dx.doi.org/10.1016/0032-0633(84)90102-8), URL <http://www.sciencedirect.com/science/article/pii/0032063384901028>.
- [108] Hansen JE, Travis LD. Light scattering in planetary atmospheres. *Space Sci Rev* 1974;16(4):527–610. <http://dx.doi.org/10.1007/BF00168069>.

- [109] Tran H, Ngo NH, Hartmann J-M. Efficient computation of some speed-dependent isolated line profiles. *J Quant Spectrosc Radiat Transfer* 2013;129:199–203. <http://dx.doi.org/10.1016/j.jqsrt.2013.06.015>.
- [110] Gamache RR, Vispoel B, Rey M, Nikitin A, Tyuterev V, Egorov O, Gordon IE, Boudon V. Total internal partition sums for the HITRAN2020 database. *J Quant Spectrosc Radiat Transfer* 2021;271:107713. <http://dx.doi.org/10.1016/j.jqsrt.2021.107713>.
- [111] Zaghoul MR, Ali AN. Algorithm 916: Computing the faddeyeva and voigt functions. *ACM Trans Math Software* 2012;38(2). <http://dx.doi.org/10.1145/2049673.2049679>.
- [112] Yamada T, Rezac L, Larsson R, Hartogh P, Yoshida N, Kasai Y. Solving non-LTE problems in rotational transitions using the Gauss-Seidel method and its implementation in the atmospheric radiative transfer simulator. *Astron Astrophys* 2018;619:A181. <http://dx.doi.org/10.1051/0004-6361/201833566>.
- [113] Karman T, Gordon I, van der Avoird A, Baranov YI, Boulet C, Drouin BJ, Groenenboom GC, Gustafsson M, Hartmann J-M, Kurucz RL, Rothman LS, Sun K, Sung K, Thalman R, Tran H, Whishnow EH, Wordsworth R, Vigasin AA, Volkamer R, van der Zande WJ. Update of the HITRAN collision-induced absorption section. *Icarus* in press 2019. <http://dx.doi.org/10.1016/j.icarus.2019.02.034>.
- [114] Mishchenko MI, Travis LD, Lacis AA. *Scattering, absorption, and emission of light by small particles*. Cambridge University Press; 2002.
- [115] Petty GW, Huang W. The modified gamma size distribution applied to inhomogeneous and nonspherical particles: Key relationships and conversions. *J Atmos Sci* 2011;68(7):1460–73.
- [116] Abel SJ, Boutle IA. An improved representation of the raindrop size distribution for single-moment microphysics schemes. *Q J R Meteorol Soc* 2012;138(669):2151–62.
- [117] Wang J, Dong X, Xi B, Heymsfield AJ. Investigation of liquid cloud microphysical properties of deep convective systems: 1. Parameterization raindrop size distribution and its application for stratiform rain estimation. *J Geophys Res Atm* 2016;121(18):10–739.
- [118] Marshall JS, Palmer WM. The distribution of raindrops with size. *J Meteorol* 1948;5:165–6. [http://dx.doi.org/10.1175/1520-0469\(1948\)005<0165:TDORWS>2.0.CO;2](http://dx.doi.org/10.1175/1520-0469(1948)005<0165:TDORWS>2.0.CO;2), Short Contribution.
- [119] McFarquhar GM, Heymsfield AJ. Parameterization of tropical cirrus ice crystal size distributions and implications for radiative transfer: Results from CEPEX. *J Atmos Sci* 1997;54(17):2187–200.
- [120] Field PR, Heymsfield AJ, Bansemir A. Snow size distribution parameterization for midlatitude and tropical ice clouds. *J Atmos Sci* 2007;64(12):4346–65.
- [121] Delanoë JME, Heymsfield AJ, Protat A, Bansemir A, Hogan RJ. Normalized particle size distribution for remote sensing application. *J Geophys Res Atm* 2014;119(7):4204–27.
- [122] Field PR, Heymsfield AJ, Detwiler AG, Wilkinson JM. Normalized hail particle size distributions from the T-28 storm-penetrating aircraft. *J Appl Meteorol Clim* 2019;58(2):231–45.
- [123] Milbrandt JA, Yau MK. A multimoment bulk microphysics parameterization. Part I: Analysis of the role of the spectral shape parameter. *J Atmos Sci* 2005;62(9):3051–64.
- [124] Adams IS, Bobak J. The feasibility of detecting supercooled liquid with a forward-looking radiometer. *IEEE J Sel Top Appl Rem Sens* 2018;11(6, SI):1932–8. <http://dx.doi.org/10.1109/JSTARS.2018.2844684>, Publisher: Institute of Elect & Electron Engineers Geoscience & Remote Sensing Soc; IEEE; IEEE GRSS.
- [125] Bohren CF, Clothiaux EE. *Fundamentals of atmospheric radiation*. WILEY-VCH Verlag GmbH & Co. KGaA; 2006, ISBN 3-527-40503-8.
- [126] Liou K. *An introduction to atmospheric radiation*. second ed.. Elsevier Science (USA); 2002, ISBN 0-12-451451-0.
- [127] Thomas GE, Stamnes K. *Radiative Transfer in the Atmosphere and Ocean*. Cambridge University Press; 1999, ISBN 0-521-89061-6.
- [128] Goody RM, Yung YL. *Atmospheric radiation: Theoretical basis*. second ed.. Oxford University Press; 1989, ISBN 0-19-510291-6.
- [129] Laszlo I, Stamnes K, Wiscombe WJ, Tsay S-C. The discrete ordinate algorithm, DISORT for radiative transfer. In: Kokhanovsky A, editor. *Light scattering reviews, volume 11: light scattering and radiative transfer*. Springer Berlin Heidelberg; 2016, p. 3–65. [http://dx.doi.org/10.1007/978-3-662-49538-4\\_1](http://dx.doi.org/10.1007/978-3-662-49538-4_1).
- [130] Evans KF, Stephens GL. *Microwave radiative transfer through clouds composed of realistically shaped ice crystals. Part II. Remote sensing of ice clouds*. *J Atmos Sci* 1995;52(11):2058–72.
- [131] Fox S. An evaluation of radiative transfer simulations of cloudy scenes from a numerical weather prediction model at sub-millimetre frequencies using airborne observations. *Rem Sens* 2020;12(17). <http://dx.doi.org/10.3390/rs12172758>.
- [132] Battaglia A, Tanelli S, Kobayashi S, Zrnic D, Hogan RJ, Simmer C. Multiple-scattering in radar systems: A review. *J Quant Spectrosc Radiat Transfer* 2010;111(6):917–47.
- [133] Oguchi T, Ishida N, Ihara T. Effect of multiple scattering on the estimation of rainfall rates using dual-wavelength radar techniques. *IEEE T Geosci Remote* 1994;32(4):943–6. <http://dx.doi.org/10.1109/36.298023>.
- [134] Battaglia A, Ajewole MO, Simmer C. Multiple scattering effects due to hydrometeors on precipitation radar systems. *Geophys Res Lett* 2005;32(19). <http://dx.doi.org/10.1029/2005GL023810>.
- [135] Marzano FS, Roberti L, Di Michele S, Mugnai A, Tassa A. Modeling of apparent radar reflectivity due to convective clouds at attenuating wavelengths. *Radio Sci* 2003;38(1):2–1–2–16. <http://dx.doi.org/10.1029/2002RS002613>.
- [136] Roemer FE, Buehler SA, Brath M, Kluft L, John VO. Direct observation of Earth's spectral long-wave feedback parameter. *Nat Geosci* 2023;16(5):416–21. <http://dx.doi.org/10.1038/s41561-023-01175-6>.
- [137] Dacie S, Kluft L, Schmidt H, Stevens B, Buehler SA, Nowack PJ, Dietmüller S, Abraham NL, Birner T. A 1D RCE study of factors affecting the tropical tropopause layer and surface climate. *J Clim* 2019;32(20):6769–82. <http://dx.doi.org/10.1175/JCLI-D-18-0778.1>.
- [138] He H, Kramer RJ, Soden BJ, Jeevanjee N. State dependence of CO<sub>2</sub> forcing and its implications for climate sensitivity. *Nature* 2023;382(6674):1051–6. <http://dx.doi.org/10.1126/science.abq6872>.
- [139] Petty GW. *A first course in atmospheric radiation*. Sundog Publishing; 2004.
- [140] Czarnecki P, Polvani L, Pincus R. Sparse, empirically optimized quadrature for broadband spectral integration. *J Adv Model Earth Syst* 2023;15(10):e2023MS003819. <http://dx.doi.org/10.1029/2023MS003819>.
- [141] Rodgers C. *Inverse methods for atmospheric sounding: theory and practice*. vol. 2, World scientific; 2000, <http://dx.doi.org/10.1142/3171>.
- [142] Buehler SA, Eriksson P, Lemke O, Larsson R, Pfreundschuh S, Brath M. ARTS - The Atmospheric Radiative Transfer Simulator (2.6.6). 2024, <http://dx.doi.org/10.5281/zenodo.13326137>.